

Dielectric Mie Resonance-Enhanced Photocatalysis on Cuprous Oxide Nanostructures

*Aaron Wheeler^{⊥‡}, Ravi Teja A. Tirumala^{⊥‡}, Sunil Gyawali[§], Rishmali Sooriyagoda[§],
Sundaram Bhardwaj Ramakrishnan[⊥], Farshid Mohammadparast[⊥], Susheng Tan[⊥],
A. Kaan Kalkan[⊥], Alan D. Bristow^{§*}, Marimuthu Andiappan^{*⊥}*

Affiliations:

⊥ School of Chemical Engineering, Oklahoma State University, Stillwater, OK, USA.

§ Department of Physics and Astronomy, West Virginia University, Morgantown, WV, USA.

⊥ School of Mechanical and Aerospace Engineering, Oklahoma State University, Stillwater, OK, USA.

⊥ Department of Electrical and Computer Engineering and Petersen Institute of Nano Science and Engineering, University of Pittsburgh, Pittsburgh, PA, USA

‡ These authors contributed equally

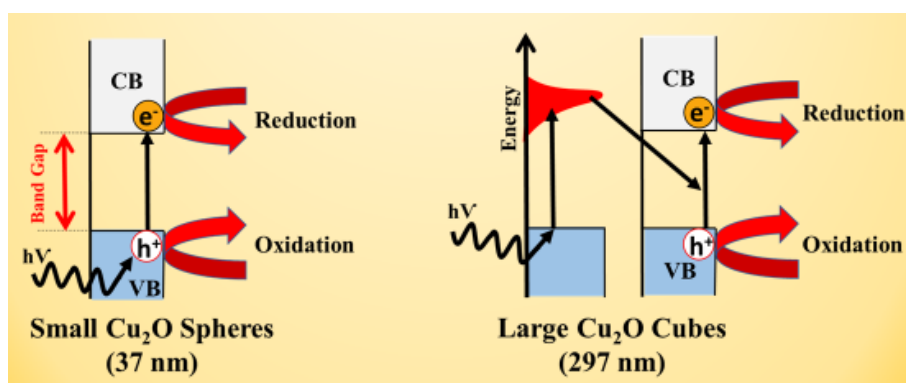
*Corresponding authors, Email: mari.andiappan@okstate.edu

KEYWORDS: Mie Resonance, Dielectric Resonance, Photocatalysis, Bandgap, Metal Oxide, Semiconductor

ABSTRACT

Nanostructured metal oxides, such as Cu_2O , CeO_2 , $\alpha\text{-Fe}_2\text{O}_3$, and TiO_2 can efficiently mediate photocatalysis for solar-to-chemical energy conversion and pollution remediation. In this contribution, we report a novel approach, dielectric resonance-enhanced photocatalysis, to enhance the catalytic activity of metal oxide photocatalysts. Specifically, we report that Cu_2O cubic particles of 297 nm edge length and spherical particles of 115 nm diameter exhibit a higher photocatalytic rate as compared to Cu_2O spherical nanoparticles of 37 nm diameter. Using transient absorption measurements, we demonstrate that the higher photocatalytic rates observed on submicron Cu_2O particles are due to a coherent electronic process that supports dielectric-resonance mediated charge carrier generation. For small Cu_2O spherical nanoparticles of 37 nm diameter, the dielectric resonances are absent. Although we demonstrated the concept using Cu_2O particles, our FDTD simulations predict that this concept can be broadly applied to other metal oxide photocatalysts, including CeO_2 , $\alpha\text{-Fe}_2\text{O}_3$ and TiO_2 .

TOC GRAPHICS



MAIN TEXT

Ever since the discovery of titanium dioxide (TiO₂) semiconductor-based photo-electrochemistry for water splitting by Fujishima and Honda in 1972, they have opened the gateway for semiconductor-assisted photocatalysis.¹ The idea of bandgap-facilitated photochemistry on semiconductors has been the basis for research over the next five decades. In bandgap-facilitated photocatalysis on semiconductors, the photo-excited electrons and holes can drive reduction and oxidation reactions, respectively (Figure 1a). The excited electron-driven reduction of protons (H⁺) into hydrogen (H₂) and hole-driven oxidation of water into oxygen (O₂) are the examples of photon-excited charge carriers-driven chemistry.

Researchers have explored the properties of semiconductors such as cerium oxide (CeO₂), cuprous oxide (Cu₂O), hematite iron (III) oxide (α -Fe₂O₃) and TiO₂ in the last four decades for the solar-to-chemical energy and pollution mitigation applications.²⁻⁷ But some challenges still exist in using semiconductor (only)-based photocatalysts for the efficient conversion of solar energy into chemical energy. For instance, the semiconductor nanostructures lack efficient utilization of incoming photons because of their inherently poor absorption cross section.⁸ Plasmonic metal nanostructures (PMNs) have emerged as promising materials to overcome some of these limitations. Specifically, studies in the last decade have shown that hybrid and composite photocatalysts built on PMNs (e.g., Al, Ag, Au, and Cu) and metal oxide semiconductors (e.g., Cu₂O, α -Fe₂O₃, and TiO₂) can exhibit enhanced photocatalytic activity as compared to semiconductor (only) photocatalysts.⁸⁻¹⁵

The absorption cross sections of PMNs are four to five orders of magnitude higher than dye molecules.¹⁶ This strong interaction of PMNs with the incident ultraviolet/visible (UV/Vis) light is due to the localized surface plasmon resonance (LSPR).¹⁶⁻¹⁸ The PMN can therefore efficiently

harvest the incident light and transfer the energy into the nearby metal oxide semiconductor via a number of electron- and energy-transfer pathways, including plasmon-induced hot electron transfer, nanoantenna effect, and plasmon-induced resonance energy transfer (Figure 1b).⁸⁻¹¹ The plasmonic resonance-mediated energy transfer from PMN into the nearby metal oxide semiconductor can result in an enhanced rate of formation of excited electrons and holes in the conduction and valence bands of the semiconductor, respectively (Figure 1b).⁹ These enhanced rates of formation of charge carriers are shown to result in enhanced photocatalytic activity in PMN-metal oxide composite photocatalysts.^{8-12,19} In our previous contribution,²⁰ we have reported that similar to the plasmonic resonances in PMNs, tunable dielectric resonances can be created in metal oxide particles by controlling their size and shape. Herein, we demonstrate that these dielectric resonances can be utilized to enhance the inherent photocatalytic activity of metal oxide photocatalysts (Figure 1c). In the plasmonic resonance-mediated photocatalytic approach shown in Figure 1b, two building blocks are required: PMN to facilitate the plasmonic resonance and semiconductor for the bandgap-facilitated reduction and oxidation (redox) reactions. In contrast, in the proposed dielectric resonance-mediated photocatalytic approach shown in Figure 1c, a single metal oxide building block can serve the dual function and exhibit both the dielectric resonance behavior and the bandgap-facilitated redox reactions.

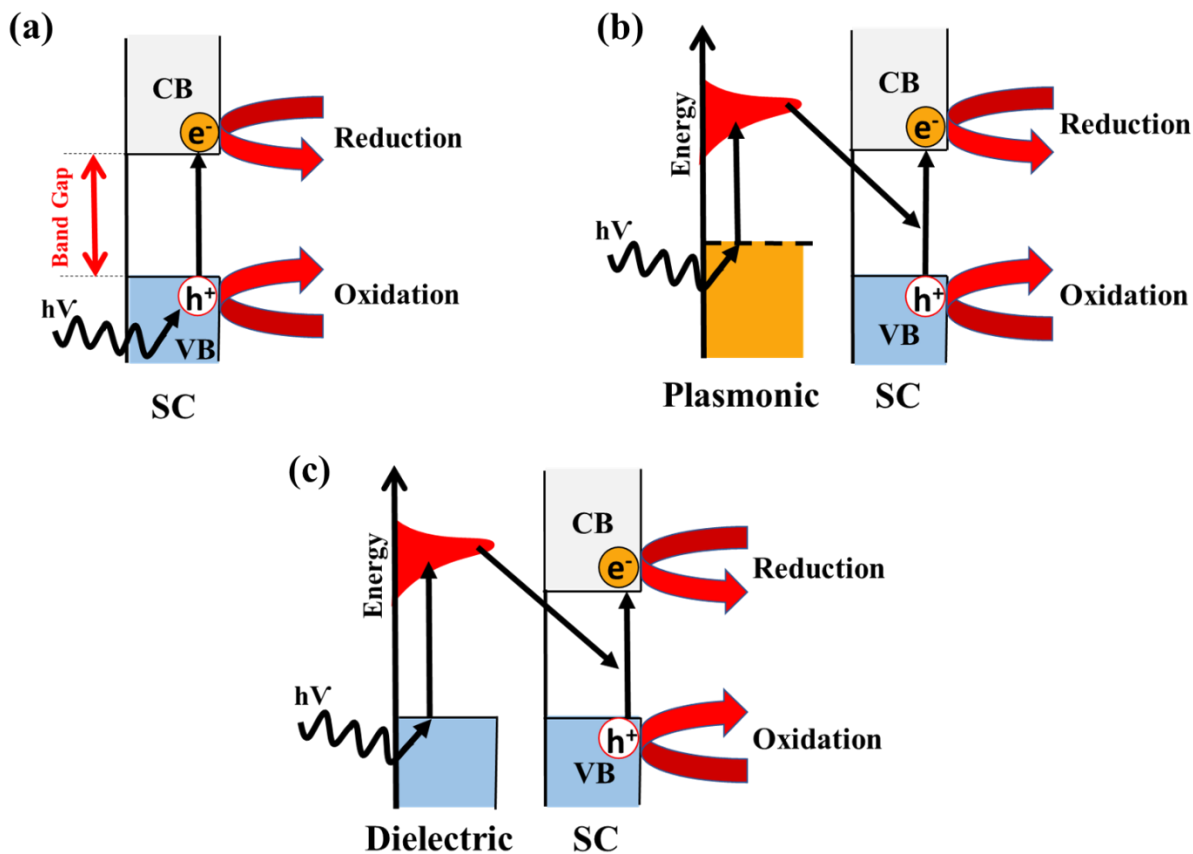


Figure 1. Schematic diagram illustrating (a) formation of photoexcited electrons (e^-) and holes (h^+) in semiconductor (SC), (b) plasmonic resonance-mediated formation of excited electrons and holes in SC, and (c) the proposed dielectric resonance-mediated formation of excited electrons and holes in SC. In (a), (b), and (c), excited electrons in the conduction band (CB) and excited holes in the valence band (VB) of SC can drive reduction and oxidation reactions.

The plasmonic and dielectric resonances are two distinct sub-categories of Mie resonances.^{21,22} The plasmonic resonances occur for materials with negative values of the real part of the permittivity ($\epsilon < 0$). The Mie resonances can also occur for materials with positive values of permittivity ($\epsilon > 0$). When Mie resonances occur in the positive permittivity region, the resonances

are known as dielectric resonances. Specifically, dielectric resonances can occur in materials with moderate (2.5-3.5) and high refractive index (>3.5).²³ Compared to plasmonic, Mie resonances which exhibit only the electric multipole resonances (e.g., electric dipole, quadrupole. etc.), the dielectric Mie resonances can exhibit electric and magnetic multipole resonances upon light excitation.²⁰ Similar to the plasmonic resonances, the dielectric resonance wavelengths are also tunable with the size and shape of the particle.²⁰ At the resonance wavelengths, the dielectric nanostructures can act as optical nanoantenna and exhibit orders of magnitude enhancements for the electric and magnetic fields of the incident light. The nanoantenna and light trapping effects of dielectric nanostructures are utilized for dielectric resonance-enhanced light absorption, fluorescence, and Raman scattering.²¹ For example, dielectric Mie resonances have been demonstrated for their use in controlling and enhancing light absorption for solar fuel generation and thin-film solar cell applications.^{24,25}

The dielectric resonances can also result in the appearance of Mie absorption peaks in the UV-Vis-near infrared (UV-Vis-near IR) absorption spectra of medium- and high-refractive index dielectric particles.²⁰ These Mie absorption peaks, which are not present in their bulk counterparts, provide an opportunity for enhanced light harvesting capability in dielectric particles. For example, FeS₂ nanocubes with dielectric Mie absorption have been demonstrated to exhibit a higher photothermal conversion efficiency as compared to the small FeS₂ nanoparticles not exhibiting dielectric Mie absorption.²⁶ Herein, we demonstrate that submicron Cu₂O cubic particles with dielectric Mie absorption peaks exhibit a higher photocatalytic rate as compared to small Cu₂O spherical nanoparticles not exhibiting dielectric Mie resonances.

Cu₂O is a semiconductor with a bandgap of ~ 2.1 eV.^{5-7,27} It is also a moderate refractive index material with the values of the real part of the refractive index in the range of $\sim 2.6 - 3.1$ (SI).²⁰

Cu₂O is also known for exhibiting a relatively long lifetime of excited charge carriers (electrons and holes) that is on the order of milliseconds.^{28,29} In our previous contribution²⁰, we have demonstrated that: (i) submicron Cu₂O cubic particles of edge lengths greater than ~ 100 nm exhibit strong dielectric resonances in the Vis-near IR regions, (ii) the dielectric resonance strengths of these Cu₂O cubic particles are similar to or greater than plasmonic resonances of Ag particles of similar sizes, and (iii) small Cu₂O spherical and cubic particles of sizes less than 100 nm exhibit light absorption features similar to their bulk counterparts and does not exhibit any Mie resonances in the Vis-near IR regions. In this contribution, we demonstrate that large Cu₂O cubic particles of 297 nm average edge length exhibit higher visible-light photocatalytic activity for methylene blue (MB) dye degradation as compared to small Cu₂O spherical nanoparticles of 37 nm average diameter. We attribute the higher photocatalytic rate of large Cu₂O cubes to their dielectric Mie resonances, which are not present in the small Cu₂O spheres. The results from the photoreactor studies are supported by the transient-absorption measurements that are used to identify the incoherent or coherent charge carrier dynamics that are markedly different for the small Cu₂O spheres and large Cu₂O cubes.

Syntheses and characterizations of small Cu₂O spheres, large Cu₂O spheres, and large Cu₂O cubes: Microemulsion technique^{30,31} is used for the synthesis of small Cu₂O spheres. For the syntheses of large Cu₂O spheres and cubes, chemical reduction method²⁰ is used. The detailed procedures followed for the syntheses and characterizations of Cu₂O particles, and finite-difference time-domain (FDTD) simulations, photocatalytic experiments, and transient absorption measurements are provided in the supporting information (SI).

Figure 2a and Figure 2b show the representative TEM images of large Cu₂O nanocubes of 297 nm average edge length and small Cu₂O spheres of 37 nm average diameter, respectively. The Cu₂O

phase of these cubical and spherical particles are confirmed using the XRD analysis of the respective particles (e.g., Figure S1b and Figure S1c in SI). The photocatalytic performances of large Cu₂O nanocubes and small Cu₂O nanospheres towards MB degradation are evaluated under visible light irradiation. In these studies, the photocatalytic MB dye degradations are carried out for the same weight load of small Cu₂O spheres and large Cu₂O cubes. The blue and green LED lamps that emit light with peak wavelengths at 456 and 519 nm, respectively, are used as the visible light source. In Figure 2c, we provide the spectrum of blue and green LEDs and the absorption spectrum of MB. As seen from Figure 2c, there is minimal overlap between the spectrum of the light source (i.e., blue and green LEDs) and the absorption spectrum of methylene blue. This minimal overlap will ensure that the MB dye degradation due to direct dye excitation is minimal. In Figure 2d, we show the extent of MB dye degradation (i.e., ratio of concentration of MB to its initial concentration, C/C_0) by large Cu₂O cubes and small Cu₂O spheres as a function of visible light irradiation time. As seen from Figure 2d, large Cu₂O nanocubes exhibit a significantly higher MB degradation rate than small Cu₂O nanospheres. We also performed photocatalytic experiments under visible light irradiation in the absence of Cu₂O particles and found no significant MB degradation under these blank conditions (Figure 2d).

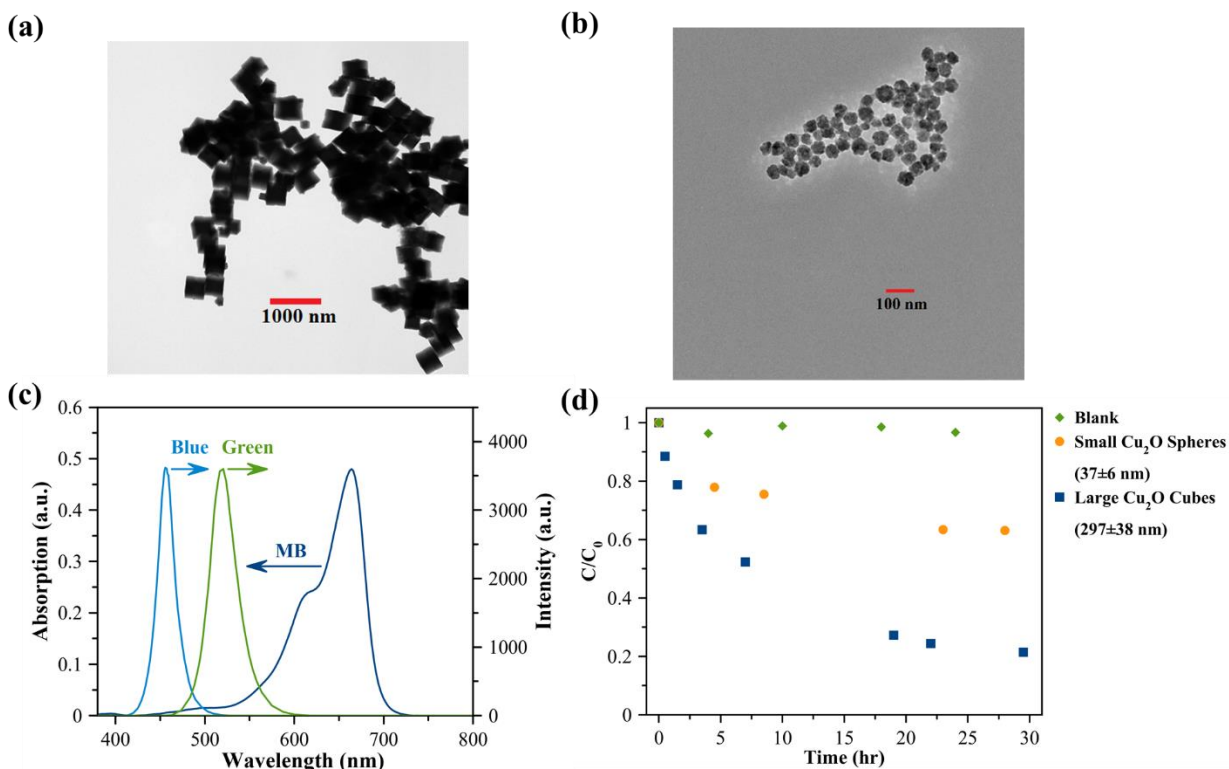


Figure 2. Representative TEM images of (a) large Cu₂O nanocubes of 297 ± 38 nm edge length, and (b) small Cu₂O nanospheres of 37 ± 6 nm diameter. (c) Absorption spectrum of MB (left ordinate) and spectrum of blue and green LED light source used for photocatalytic degradation of MB (right ordinate). (d) Plot of C/C_0 versus irradiation time for photocatalytic degradation of MB in ethanol using large Cu₂O nanocubes (blue squares), small Cu₂O nanospheres (orange circles), and under blank conditions in the absence of photocatalyst (green diamonds).

To confirm that the MB degradations shown in Figure 2d are not due to the light-induced heating effect, we measured the change in temperature of the reaction mixture as a function of irradiation time. We found that visible light irradiation increases the temperature of the reaction mixture from ~ 20 °C to a maximum of ~ 31 °C (Figure S2a-c in SI). Specifically, we observed a similar extent of increase in temperature for the photocatalytic experiments performed using small Cu₂O spheres,

large Cu₂O cubes, and under blank conditions in the absence of Cu₂O particles (Figure S2a-c in SI). The heat localization in our system is also expected to be minimal since the photocatalytic experiments are performed in the liquid medium under stirring.³² We also carried out heating experiments in the presence of large Cu₂O cubes under dark conditions. In these heating experiments, the temperature of the reaction mixture is maintained at 60 °C. For all tested experimental conditions, the heating trials revealed no significant MB degradation in the absence of light exposure across an extended period (Figure S2d in SI).

To show that the higher photocatalytic rates of large Cu₂O cubes in Figure 2d are due to their dielectric Mie resonances, in Figure 3a, we show the UV-Vis extinction spectra of large Cu₂O cubes and small Cu₂O spheres. As seen from Figure 3a, small Cu₂O spheres, in consistent with what is expected for their bulk counterparts, exhibit no resonance peaks in the UV-Vis-near IR extinction spectra. In contrast, large Cu₂O cubes exhibit multiple resonance peaks in the visible to near IR regions. To understand the nature of these resonance peaks, we performed FDTD simulations of Cu₂O spherical particle of 37 nm diameter and Cu₂O cubical particle of 297 nm. The simulated extinction spectra of these particles are shown in Figure S3a in SI. The features observed in the simulated extinction spectra of small Cu₂O spheres and large Cu₂O cubes are consistent with the experimentally measured extinction spectra of the respective Cu₂O particles shown in Figure 3a. The magnetic and electric field distributions at different wavelengths across the resonance peaks of the Cu₂O cubes of 297 nm edge length are also provided in Figure S3b-c in SI. The field distributions confirm that the resonance peaks observed in the extinction spectra of the Cu₂O cube are due to the dielectric Mie resonances.²⁰ From the field distribution maps, we assign the lowest energy resonance peak observed in the extinction spectrum of the Cu₂O cube to the combination of electric and magnetic dipoles (Figure S3b-c in SI).²⁰ Similarly, we assign the

second lowest energy resonance peak and higher-order resonance peaks to the combination of electric and magnetic quadrupoles and the combination of higher-order electric and magnetic resonance modes, respectively.²⁰

In Figure 3b, we show the simulated absorption spectra of small Cu₂O spheres and large Cu₂O cubes. The y-axis values in the figure correspond to the volume-normalized absorption cross section. This normalized absorption cross section is a good descriptor to predict the relative photocatalytic rates of large Cu₂O cubes and small Cu₂O spheres (see SI for more details). Also, the wavelengths of interest for comparison are in the range of 400-600 nm since the blue and green LEDs used in our system cover this wavelength region. As seen from Figure 3b, in the 400-600 nm wavelengths region, large Cu₂O cubes exhibit relatively higher overall light absorption capacity than small Cu₂O spheres. Specifically, the higher-order dielectric Mie resonances in the Cu₂O cube provide enhanced overall light absorption capacity in the 400-600 nm region. Therefore, we attribute the enhanced photocatalytic rate of large Cu₂O cubes shown in Figure 2d to their dielectric Mie resonances-mediated Mie absorption, which is absent in small Cu₂O spheres. To compare and confirm this Mie resonance effect in Cu₂O particles of the same shape, we carried out photocatalytic experiments using large spherical particles of 115 ± 25 nm diameter. We find that these large spherical particles of 115 nm average diameter exhibit dielectric Mie resonance peaks and a higher photocatalytic rate as compared to small Cu₂O spherical nanoparticles not exhibiting dielectric Mie resonances (Figure S3d-f in SI).

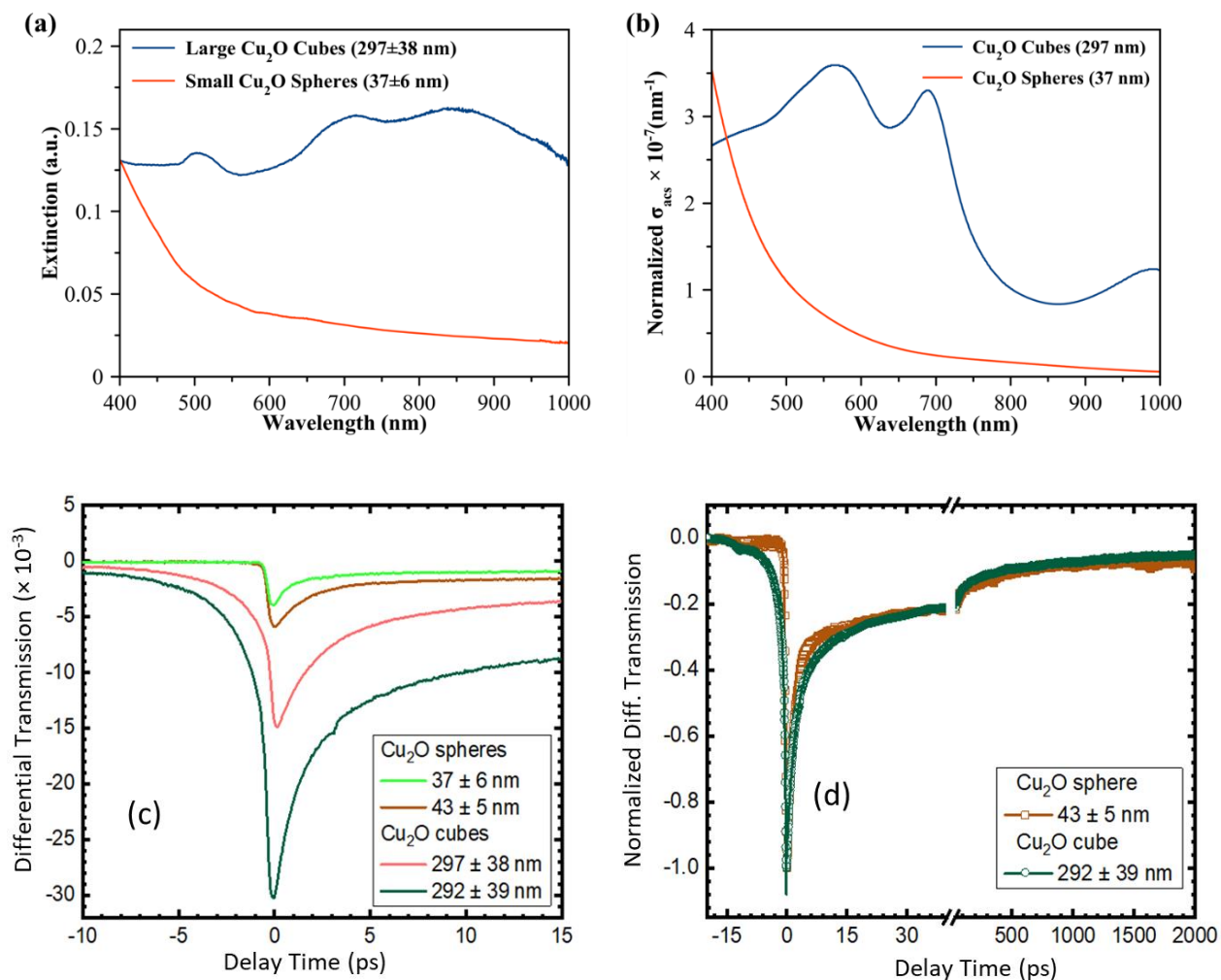


Figure 3. (a) Experimentally measured UV-Vis-near IR extinction spectra of large Cu₂O nanocubes of 297 ± 38 nm edge length and small Cu₂O nanospheres of 37 ± 6 nm diameter dispersed in ethanol. (b) FDTD-simulated normalized absorption cross section (normalized σ_{acs}) as a function of incident light wavelength for a large Cu₂O nanocube of 297 nm edge length and a small Cu₂O nanosphere of 37 nm diameter. (c) Temporal response of the differential transmission of small Cu₂O spheres of 37 ± 6 nm and 43 ± 5 nm diameters and large Cu₂O cubes of 297 ± 38 nm and 292 ± 39 nm edge lengths. (d) Temporal response of the normalized differential transmission with exponential fits overlaid for small Cu₂O spheres of 43 ± 5 nm diameter and large

Cu₂O cubes of 292 ± 39 nm edge length. A pump pulse of 400 nm wavelength and a probe pulse of 800 nm wavelength are used in (c) and (d).

To further illustrate the Mie resonance-mediated photocatalysis, we show the transient absorption spectra of large Cu₂O cubes and small Cu₂O spheres in Figure 3c-d. Specifically, Figure 3c shows the transients for short time periods for two sets of small Cu₂O spheres of 37 ± 6 nm and 43 ± 5 nm diameters and two sets of large Cu₂O cubes of 297 ± 38 nm and 292 ± 39 nm edge lengths. Using the pump and probe conditions described in the methods section, the excitation in either sample is sufficiently above any absorption edge of the Cu₂O, creating excited-state charge carriers. The probe pulse then senses the excited-state carriers through free-carrier absorption of the pumped carriers, pushing them further into their respective bands. For the positive delay time both small Cu₂O spheres and large Cu₂O cubes exhibit a three-component exponential decay with typical delay times corresponding to a few picoseconds, a few tens of picoseconds, and a few hundred picoseconds. Fits are overlaid on the transient-absorption data shown for the full-data range for one of each sample type in Figure 3d and extracted parameters are given in Table 1.

Markedly, the negative delay time response from the large Cu₂O cubes does not have the fast rise that is seen exhibited by the small Cu₂O spheres. In the latter, the rise is limited to the autocorrelation of the pump and probe pulses in the sample, typically the same order of magnitude as the laser pulse width (~ 100 fs). The response of large Cu₂O cubes is indicative of a coherent response, like that seen as perturbed free induction in bleachable dyes,³³ GaAs quantum well,³⁴ single interfacial quantum dots,³⁵ and Au@SiO₂@Cu₂O core-shell nanoparticles that demonstrate plasmon-induced resonance energy transfer (PIRET, Figure 1b).⁹ Experimentally, these processes are observed because the weaker probe pulse imparts its coherent wavefront into the samples,

which evolves over time, but has sufficient “*memory*” to then scatter some of the stronger pump light into the probe-detection direction, hence making this coherent process visible during negative delay times. The negative delay time response is fit with a double exponential decay, which reveals a faster component of a similar rise time as that of the nanospheres, which do not exhibit the protracted rise and a slower (~5 ps) response that is associated with the coherent energy transfer mechanism. Extracted fit parameters are also shown in Table 1.

Table 1. Extracted fitting parameters for the differential transmission data.

Cu ₂ O Sample	t _{r1} (ps)	t _{r2} (ps)	t _{d1} (ps)	t _{d2} (ps)	t _{d3} (ps)
Spheres (37 ± 6 nm)	0.41	-	0.36	34.0	2282.9
Spheres (43 ± 5 nm)	0.64	-	0.95	40.0	2073.6
Cubes (292 ± 39 nm)	0.72	5.4	2.37	37.1	669.6
Cubes (297 ± 38 nm)	0.53	4.5	2.43	37.5	672.0

The coherent signature observed in the transient absorption of large Cu₂O cubes is expected because the dielectric Mie resonance-mediated charge carriers generation in dielectric Cu₂O particles (Figure 1b) is most likely a coherent process, in a similar way to the PIRET-mediated charge carriers generation in the Cu₂O shell of Au@SiO₂@Cu₂O core-shell nanoparticles (Figure 1b).⁹ Hence, the results of transient absorption measurements shown in Figure 3c-d and Table 1 provide direct evidence of a coherent process in the large Cu₂O cubes.

To illustrate the photocatalytic mechanism that is responsible for the MB degradation on large Cu₂O cubes, we investigated the possible role of the solvent and superoxide (O₂⁻) on the MB degradation. To investigate the solvent dependency on the MB degradation, we performed photocatalytic experiments using two different solvents, dimethylformamide (DMF) and ethanol,

and the representative results are shown in Figure 4a. In the solvent-dependent studies, Cu₂O cubes exhibited a similar or slightly faster MB degradation in DMF compared to ethanol. We attribute the observed slightly faster MB degradation to the expected higher solubility of dissolved oxygen in DMF compared to ethanol. Previous studies have demonstrated that MB degradation on semiconductor photocatalysts can occur via a superoxide-mediated mineralization mechanism.^{36,37} To investigate whether the photocatalytic MB degradation occurs via a superoxide-mediated mechanism, we performed the photocatalytic experiments with and without benzoquinone, a well-known scavenger of the superoxide.³⁸ The results from these experiments are shown in Figure 4b. The direct evidence of the superoxide-mediated mechanism can be gathered from Figure 4b, with the benzoquinone successfully inhibiting the MB degradation via scavenging of the superoxide. Based on these findings, we propose the following photocatalytic mechanism for the MB degradation on large Cu₂O cubes. This mechanism, schematically illustrated in Figure 4c, involves the excitation of dielectric Mie resonances by the incident photons. The energy stored in Mie extinction dissipates into Mie scattering and Mie absorption. A major fraction of the energy that corresponds to Mie absorption transfers into and results in the coherent generation of excited electrons (e⁻) and holes (h⁺) in the conduction and valence bands of Cu₂O, respectively. The excited electrons from the conduction band reduce the dissolved oxygen (O₂) into superoxide (O₂⁻). The superoxide then reacts with the MB molecule and forms several intermediate products, one of them being a carboxylic acid (RCOO⁻) intermediate.^{36,37} This intermediate can be oxidized by the excited hole (h⁺) in the valence band into degradation products.^{36,37}

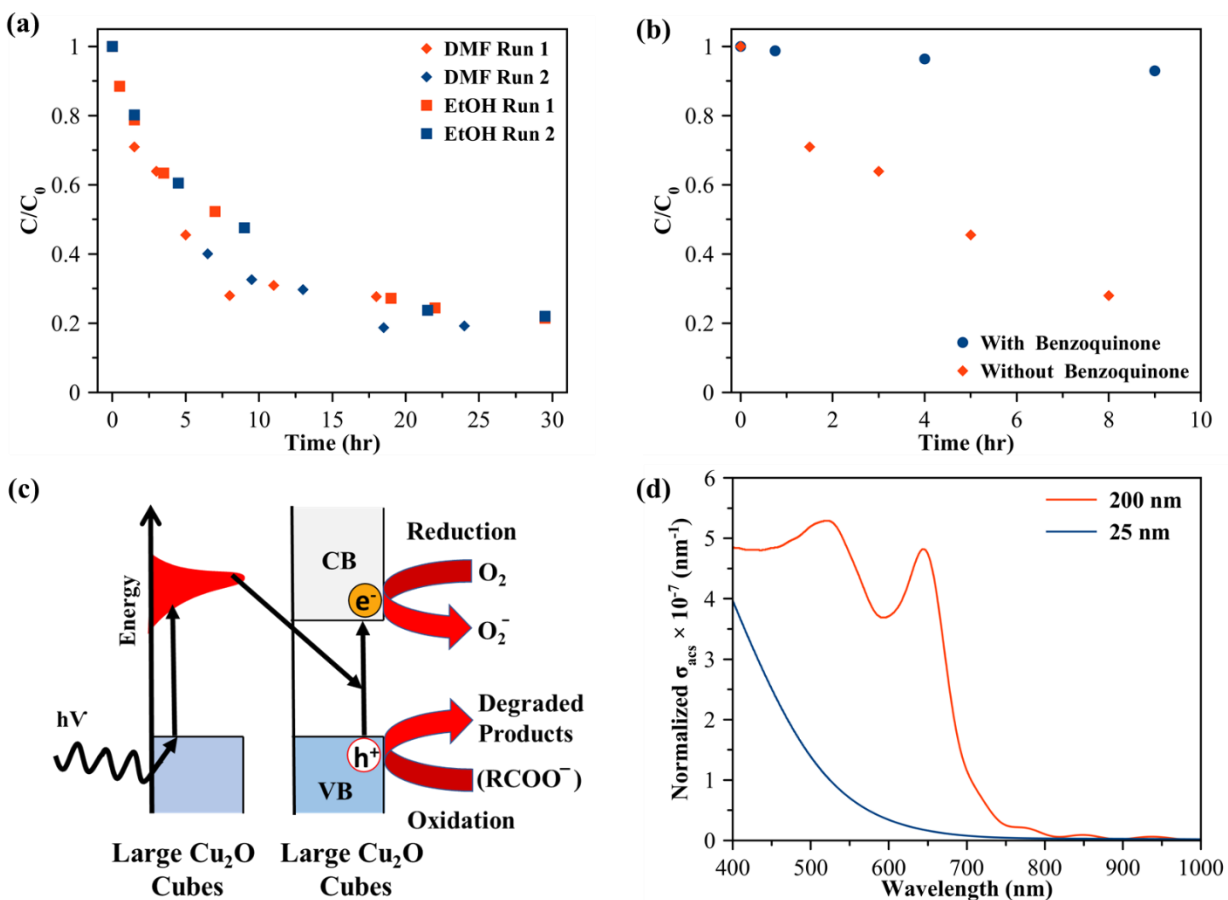


Figure 4. (a) Plot of C/C_0 versus irradiation time for photocatalytic degradation of MB in ethanol (red and blue squares) and DMF (red and blue diamonds) using large Cu_2O nanocubes. (b) Plot of C/C_0 versus irradiation time for photocatalytic degradation of MB in the presence (blue circles) and absence (red diamonds) of benzoquinone using large Cu_2O nanocubes in DMF. (c) Schematic diagram illustrating the proposed dielectric resonance-enhanced photocatalytic degradation of MB that occurs via a superoxide (O_2^-)-mediated mechanism. (d) FDTD-simulated normalized absorption cross section (normalized σ_{acs}) as a function of incident light wavelength for a large $\alpha\text{-Fe}_2\text{O}_3$ nanosphere of 300 nm diameter and a small $\alpha\text{-Fe}_2\text{O}_3$ nanosphere of 10 nm diameter.

The dielectric resonance-enhanced photocatalytic approach demonstrated herein can be potentially applied to other metal oxide photocatalysts. For example, CeO_2 , $\alpha\text{-Fe}_2\text{O}_3$, and TiO_2 semiconductors are also moderate and high refractive index materials with the values of the real part of the refractive index in the range of 2.1-2.5, 2.7-3.3, and 1.4-5.4, respectively (SI). To investigate whether these metal oxide particles exhibit dielectric resonance characteristics similar to that of Cu_2O , we performed FDTD simulations to simulate the absorption spectra of different sizes of CeO_2 , $\alpha\text{-Fe}_2\text{O}_3$, and TiO_2 particles. The representative spectra are shown in Figure 4d and also in Figure S4a-c in SI. Our FDTD simulations show that CeO_2 , $\alpha\text{-Fe}_2\text{O}_3$, and TiO_2 particles exhibit dielectric resonance characteristics that are similar to Cu_2O particles. Specifically, our findings show that small nanoparticles such as spherical nanoparticles of 25 nm diameter exhibit light absorption features similar to their bulk counterparts and do not exhibit any Mie resonances in the near UV-Vis-near IR regions. In contrast, large nanoparticles such as spherical nanoparticles of 200 nm diameters exhibit strong dielectric resonances. For example, Figure 4d shows the normalized absorption cross section values as a function of incident light wavelengths for 25 and 200 nm spherical $\alpha\text{-Fe}_2\text{O}_3$ particles. As seen from Figure 4d, in the visible region, 200 nm spherical particle exhibits relatively higher light absorption capacity than small spheres of 25 nm diameter. Similar to the dielectric resonance-enhanced photocatalysis demonstrated in larger Cu_2O cubic particles in this contribution, the dielectric resonance features of larger CeO_2 , $\alpha\text{-Fe}_2\text{O}_3$, and TiO_2 particles can be possibly explored to enhance their inherent photocatalytic activity. We also used this rational approach to develop structure-performance relationship between the size of Cu_2O spheres and cubes and their photocatalytic performance. The results are shown in Figure 5. The weight load of NPs was kept constant in these experiments. As seen from Figure 5, our simulation

as well as experimental results predict a volcano-type relationship between the photocatalytic rate and the size of Cu₂O nanostructures.

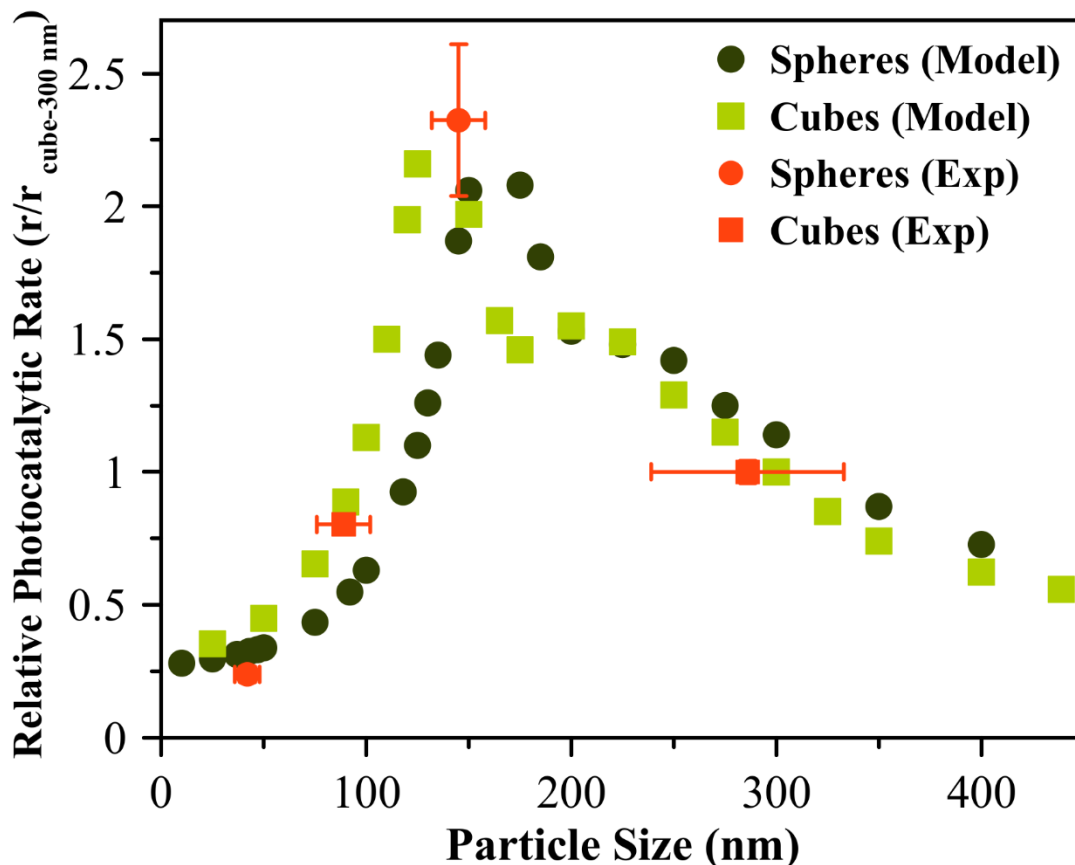


Figure 5. Volcano plot showing the predicted and experimentally measured relative photocatalytic rate as a function of size of Cu₂O spheres and cubes. Cu₂O cubes of 292 nm average edge length is used as a reference.

In conclusion, the present work demonstrates dielectric resonance-enhanced photocatalysis in submicron Cu₂O cubical and spherical particles. Specifically, submicron Cu₂O particles with dielectric resonances exhibit a higher photocatalytic rate for MB degradation in comparison to small Cu₂O spherical nanoparticles not exhibiting dielectric resonances. These results are supported by the transient absorption measurements that differentiate the charge carrier dynamics

of large Cu₂O cubes and small Cu₂O nanospheres, indicating an optical resonance process that involves the coherent generation of charge carriers in the submicron cubes. The dielectric resonance-enhanced photocatalytic approach demonstrated in this study using Cu₂O particles is expected to translate to other metal oxide photocatalysts such as CeO₂, α -Fe₂O₃, and TiO₂ that exhibit size- and shape-dependent dielectric resonances. The dielectric Mie resonance-mediated charge carrier generation in the metal oxide semiconductors has a number of advantages over plasmonic resonance-mediated charge carrier generation. Specifically, in the latter case, the plasmonic Mie mode decays to a hot electron (and hole). In comparison to the lifetime of hot electron (and hole), the electron-hole pair lifetime in the metal oxide semiconductor is longer, which will translate to a much more efficient photocatalysis. Therefore, the dielectric resonance-enhanced photocatalysis demonstrated in our study opens a new avenue for solar light harvesting and photocatalysis.

ASSOCIATED CONTENT

Supporting Information

Detailed descriptions of photocatalysts syntheses and characterization procedures, photocatalytic experimental procedures, transient absorption measurements, FDTD simulations and supporting figures are listed and supplied in Supporting Information.

AUTHOR INFORMATION

***Corresponding authors, Email: mari.andiappan@okstate.edu**

References:

- (1) Fujishima, A.; Honda, K. Electrochemical Photolysis of Water at a Semiconductor Electrode. *Nature* **1972**, *238* (5358), 37–38. <https://doi.org/10.1038/238037a0>.
- (2) Serpone, N.; Emeline, A. V. Semiconductor Photocatalysis — Past, Present, and Future Outlook. *J. Phys. Chem. Lett.* **2012**, *3* (5), 673–677. <https://doi.org/10.1021/jz300071j>.
- (3) Ma, R.; Zhang, S.; Wen, T.; Gu, P.; Li, L.; Zhao, G.; Niu, F.; Huang, Q.; Tang, Z.; Wang, X. A Critical Review on Visible-Light-Response CeO₂-Based Photocatalysts with Enhanced Photooxidation of Organic Pollutants. *Catalysis Today* **2019**, *335*, 20–30. <https://doi.org/10.1016/j.cattod.2018.11.016>.
- (4) Tamirat, A. G.; Rick, J.; Dubale, A. A.; Su, W.-N.; Hwang, B.-J. Using Hematite for Photoelectrochemical Water Splitting: A Review of Current Progress and Challenges. *Nanoscale Horiz.* **2016**, *1* (4), 243–267. <https://doi.org/10.1039/C5NH00098J>.
- (5) Bagal, I. V.; Chodankar, N. R.; Hassan, M. A.; Waseem, A.; Johar, M. A.; Kim, D.-H.; Ryu, S.-W. Cu₂O as an Emerging Photocathode for Solar Water Splitting - A Status Review. *International Journal of Hydrogen Energy* **2019**, *44* (39), 21351–21378. <https://doi.org/10.1016/j.ijhydene.2019.06.184>.
- (6) Hara, M.; Kondo, T.; Komoda, M.; Ikeda, S.; Kondo, J. N.; Domen, K.; Hara, M.; Shinohara, K.; Tanaka, A. Cu₂O as a Photocatalyst for Overall Water Splitting under Visible Light Irradiation. *Chem. Commun.* **1998**, No. 3, 357–358. <https://doi.org/10.1039/a707440i>.
- (7) Kumar, S.; Parlett, C. M. A.; Isaacs, M. A.; Jowett, D. V.; Douthwaite, R. E.; Cockett, M. C. R.; Lee, A. F. Facile Synthesis of Hierarchical Cu₂O Nanocubes as Visible Light Photocatalysts. *Applied Catalysis B: Environmental* **2016**, *189*, 226–232. <https://doi.org/10.1016/j.apcatb.2016.02.038>.
- (8) Linic, S.; Christopher, P.; Ingram, D. B. Plasmonic-Metal Nanostructures for Efficient Conversion of Solar to Chemical Energy. *Nature Mater* **2011**, *10* (12), 911–921. <https://doi.org/10.1038/nmat3151>.
- (9) Li, J.; Cushing, S. K.; Meng, F.; Senty, T. R.; Bristow, A. D.; Wu, N. Plasmon-Induced Resonance Energy Transfer for Solar Energy Conversion. *Nature Photonics* **2015**, *9* (9), 601–607. <https://doi.org/10.1038/nphoton.2015.142>.
- (10) Hou, W.; Cronin, S. B. A Review of Surface Plasmon Resonance-Enhanced Photocatalysis. *Adv. Funct. Mater.* **2013**, *23* (13), 1612–1619. <https://doi.org/10.1002/adfm.201202148>.
- (11) Cushing, S. K.; Wu, N. Progress and Perspectives of Plasmon-Enhanced Solar Energy Conversion. *J. Phys. Chem. Lett.* **2016**, *7* (4), 666–675. <https://doi.org/10.1021/acs.jpcclett.5b02393>.
- (12) DeSario, P. A.; Pietron, J. J.; Dunkelberger, A.; Brintlinger, T. H.; Baturina, O.; Stroud, R. M.; Owrutsky, J. C.; Rolison, D. R. Plasmonic Aerogels as a Three-Dimensional Nanoscale Platform for Solar Fuel Photocatalysis. *Langmuir* **2017**, *33* (37), 9444–9454. <https://doi.org/10.1021/acs.langmuir.7b01117>.
- (13) Link, S.; Masiello, D. J. Introduction: Plasmonics in Chemistry. *Chem. Rev.* **2018**, *118* (6), 2863–2864. <https://doi.org/10.1021/acs.chemrev.8b00146>.
- (14) Brongersma, M. L.; Halas, N. J.; Nordlander, P. Plasmon-Induced Hot Carrier Science and Technology. *Nature Nanotech* **2015**, *10* (1), 25–34. <https://doi.org/10.1038/nnano.2014.311>.

- (15) Tatsuma, T.; Nishi, H.; Ishida, T. Plasmon-Induced Charge Separation: Chemistry and Wide Applications. *Chem. Sci.* **2017**, *8* (5), 3325–3337. <https://doi.org/10.1039/C7SC00031F>.
- (16) Jain, P. K.; Lee, K. S.; El-Sayed, I. H.; El-Sayed, M. A. Calculated Absorption and Scattering Properties of Gold Nanoparticles of Different Size, Shape, and Composition: Applications in Biological Imaging and Biomedicine. *J. Phys. Chem. B* **2006**, *110* (14), 7238–7248. <https://doi.org/10.1021/jp057170o>.
- (17) Zhao, T.; Herbert, P. J.; Zheng, H.; Knappenberger, K. L. State-Resolved Metal Nanoparticle Dynamics Viewed through the Combined Lenses of Ultrafast and Magneto-Optical Spectroscopies. *Acc. Chem. Res.* **2018**, *51* (6), 1433–1442. <https://doi.org/10.1021/acs.accounts.8b00096>.
- (18) Hartland, G. V.; Besteiro, L. V.; Johns, P.; Govorov, A. O. What's so Hot about Electrons in Metal Nanoparticles? *ACS Energy Lett.* **2017**, *2* (7), 1641–1653. <https://doi.org/10.1021/acsenergylett.7b00333>.
- (19) Wu, N. Plasmonic Metal–Semiconductor Photocatalysts and Photoelectrochemical Cells: A Review. *Nanoscale* **2018**, *10* (6), 2679–2696. <https://doi.org/10.1039/C7NR08487K>.
- (20) Mohammadparast, F.; Ramakrishnan, S. B.; Khatri, N.; Tirumala, R. T. A.; Tan, S.; Kalkan, A. K.; Andiappan, M. Cuprous Oxide Cubic Particles with Strong and Tunable Mie Resonances for Use as Nanoantennas. *ACS Appl. Nano Mater.* **2020**, *3* (7), 6806–6815. <https://doi.org/10.1021/acsanm.0c01201>.
- (21) Kuznetsov, A. I.; Miroshnichenko, A. E.; Brongersma, M. L.; Kivshar, Y. S.; Luk'yanchuk, B. Optically Resonant Dielectric Nanostructures. *Science* **2016**, *354* (6314), aag2472. <https://doi.org/10.1126/science.aag2472>.
- (22) Dimitrios Tzarouchis; Ari Sihvola. Light Scattering by a Dielectric Sphere: Perspectives on the Mie Resonances. *Applied Sciences* **2018**, *8* (2), 184. <https://doi.org/10.3390/app8020184>.
- (23) Sugimoto, H.; Fujii, M. Colloidal Mie Resonators for All-Dielectric Metaoptics. *Adv Photo Res* **2021**, *2* (4), 2000111. <https://doi.org/10.1002/adpr.202000111>.
- (24) Kim, S. J.; Thomann, I.; Park, J.; Kang, J.-H.; Vasudev, A. P.; Brongersma, M. L. Light Trapping for Solar Fuel Generation with Mie Resonances. *Nano Lett.* **2014**, *14* (3), 1446–1452. <https://doi.org/10.1021/nl404575e>.
- (25) Brongersma, M. L.; Cui, Y.; Fan, S. Light Management for Photovoltaics Using High-Index Nanostructures. *Nature Mater* **2014**, *13* (5), 451–460. <https://doi.org/10.1038/nmat3921>.
- (26) Sugawa, K.; Matsubara, M.; Tahara, H.; Kanai, D.; Honda, J.; Yokoyama, J.; Kanakubo, K.; Ozawa, H.; Watanuki, Y.; Kojima, Y.; Nishimiya, N.; Sagara, T.; Takase, K.; Haga, M.; Otsuki, J. Mie Resonance-Enhanced Light Absorption of FeS₂ Nanocubes in a Near-Infrared Region: Intraparticulate Synergy between Electronic Absorption and Mie Resonances. *ACS Appl. Energy Mater.* **2019**, *2* (9), 6472–6483. <https://doi.org/10.1021/acsaem.9b01060>.
- (27) Marimuthu, A.; Zhang, J.; Linic, S. Tuning Selectivity in Propylene Epoxidation by Plasmon Mediated Photo-Switching of Cu Oxidation State. *Science* **2013**, *339* (6127), 1590–1593. <https://doi.org/10.1126/science.1231631>.
- (28) Kavoulakis, G. M. Bose-Einstein Condensation of Excitons in Cu₂O. *Phys. Rev. B* **2001**, *65* (3), 035204. <https://doi.org/10.1103/PhysRevB.65.035204>.
- (29) Jolk, A.; Jörger, M.; Klingshirn, C. Exciton Lifetime, Auger Recombination, and Exciton Transport by Calibrated Differential Absorption Spectroscopy in Cu₂O. *Phys. Rev. B* **2002**, *65* (24), 245209. <https://doi.org/10.1103/PhysRevB.65.245209>.

- (30) Addanki Tirumala, R. T.; P. Dadgar, A.; Mohammadparast, F.; Ramakrishnan, S. B.; Mou, T.; Wang, B.; Andiappan, M. Homogeneous *versus* Heterogeneous Catalysis in Cu₂O Nanoparticle-Catalyzed C–C Coupling Reactions. *Green Chem.* **2019**, *21* (19), 5284–5290. <https://doi.org/10.1039/C9GC01930H>.
- (31) Pary, F. F.; Addanki Tirumala, R. T.; Andiappan, M.; Nelson, T. L. Copper(I) Oxide Nanoparticle-Mediated C–C Couplings for Synthesis of Polyphenylenediethynylenes: Evidence for a Homogeneous Catalytic Pathway. *Catal. Sci. Technol.* **2021**, *11* (7), 2414–2421. <https://doi.org/10.1039/D1CY00039J>.
- (32) Jain, P. K. Taking the Heat Off of Plasmonic Chemistry. *J. Phys. Chem. C* **2019**, *123* (40), 24347–24351. <https://doi.org/10.1021/acs.jpcc.9b08143>.
- (33) Palfrey, S. L.; Heinz, T. F. Coherent Interactions in Pump–Probe Absorption Measurements: The Effect of Phase Gratings. *J. Opt. Soc. Am. B* **1985**, *2* (4), 674. <https://doi.org/10.1364/JOSAB.2.000674>.
- (34) Joffre, M.; la Guillaume, C. B.; Peyghambarian, N.; Lindberg, M.; Hulin, D.; Migus, A.; Koch, S. W.; Antonetti, A. Coherent Effects in Pump–Probe Spectroscopy of Excitons. *Opt. Lett.* **1988**, *13* (4), 276. <https://doi.org/10.1364/OL.13.000276>.
- (35) Guenther, T.; Lienau, C.; Elsaesser, T.; Glanemann, M.; Axt, V. M.; Kuhn, T.; Eshlaghi, S.; Wieck, A. D. Coherent Nonlinear Optical Response of Single Quantum Dots Studied by Ultrafast Near-Field Spectroscopy. *Phys. Rev. Lett.* **2002**, *89* (5), 057401. <https://doi.org/10.1103/PhysRevLett.89.057401>.
- (36) Houas, A. Photocatalytic Degradation Pathway of Methylene Blue in Water. *Applied Catalysis B: Environmental* **2001**, *31* (2), 145–157. [https://doi.org/10.1016/S0926-3373\(00\)00276-9](https://doi.org/10.1016/S0926-3373(00)00276-9).
- (37) Mills, A.; Wang, J. Photobleaching of Methylene Blue Sensitised by TiO₂: An Ambiguous System? *Journal of Photochemistry and Photobiology A: Chemistry* **1999**, *127* (1–3), 123–134. [https://doi.org/10.1016/S1010-6030\(99\)00143-4](https://doi.org/10.1016/S1010-6030(99)00143-4).
- (38) Zheng, S.; Lu, J.; Shi, J.; Duan, X. Two-Dimensional Confined Electron Donor–Acceptor Co-Intercalated Inorganic/Organic Nanocomposites: An Effective Photocatalyst for Dye Degradation. *RSC Adv.* **2017**, *7* (5), 2789–2795. <https://doi.org/10.1039/C6RA25534E>.

Supporting Information

Dielectric Mie Resonance-Enhanced Photocatalysis on Cuprous Oxide Nanostructures

Aaron Wheeler[⊥] ‡, *Ravi Teja A. Tirumala*[⊥] ‡, *Sunil Gyawali*[§], *Rishmali Sooriyagoda*[§],
Sundaram Bhardwaj Ramakrishnan[⊥], *Farshid Mohammadparast*[⊥], *Susheng Tan*[†],
A. Kaan Kalkan[⊥], *Alan D. Bristow*^{§*}, *Marimuthu Andiappan*^{* ⊥}

Affiliations:

⊥ School of Chemical Engineering, Oklahoma State University, Stillwater, OK, USA.

§ Department of Physics and Astronomy, West Virginia University, Morgantown, WV, USA.

⊥ School of Mechanical and Aerospace Engineering, Oklahoma State University, Stillwater, OK, USA.

† Department of Electrical and Computer Engineering and Petersen Institute of NanoScience and Engineering, University of Pittsburgh, Pittsburgh, PA, USA.

‡ These authors contributed equally

*Corresponding authors, Email: mari.andiappan@okstate.edu

I. Syntheses and characterizations of small and large Cu₂O spherical particles and large Cu₂O cubic particles

Small Cu₂O nanoparticles of quasi-spherical shape and 37 ± 6 nm diameter were synthesized at room temperature (~ 20 °C) using the microemulsion technique. In this synthesis method, 54.5 mL of n-heptane (oil phase) and polyethylene glycol-dodecyl ether (Brij, average Mn ~ 362) as surfactant are added to a 250 mL round bottom flask and allowed to stir at 550 rpm. 5.4 mL of 0.1 M copper nitrate aqueous solution is added to this mixture and 1 M hydrazine solution (5.4 mL) is added as a reducing agent. This oil in water micro-emulsion utilizes the fact that small sizes of reverse micelles are formed in which the Cu₂O nanoparticles are formed. The mixture is allowed to stir for 12 hours after which acetone is added to break the emulsion and centrifuged. These nanoparticles are washed three times (sonicated and centrifuged) to remove the surfactant and to obtain Cu₂O spherical nanoparticles that are ready to be used as photocatalyst for methylene blue dye degradation.

Large Cu₂O cubes of 297 ± 38 nm edge length were synthesized using a chemical reduction method performed at room temperature (~ 20 °C). In this method, we first prepared a copper source of 30 mL of 0.0032 M aqueous CuCl₂ solution. This solution is put into a three-neck round bottom flask, which is put in an inert environment filled with nitrogen. We added 1 mL of 0.35 M aqueous NaOH solution to this solution at room temperature, which should result in the creation of blue-colored Cu(OH)₂ colloids almost immediately. The sodium ascorbate (reducing agent) was then added in 1 mL increments. The solution subsequently became orangish-yellow, suggesting that Cu₂O cubic particles are formed. The synthesis duration was a period of one hour after which, the Cu₂O cubes were washed using ethanol three times (sonicated and centrifuged). The catalyst is suspended in 4 mL of the reaction solvent as per the reaction procedure mentioned in section II and is ready for use in photocatalytic experiments.

The chemical reduction method at a synthesis temperature of 55 °C was used for the synthesis of large Cu₂O quasi-spherical particles of 115 ± 25 nm diameter. 50 mL of 10 mM CuCl₂ aqueous solution was prepared in a 100 mL round bottom flask. The mixture was allowed to stir at 900 rpm at 55°C. 5 mL of 2 M NaOH solution was added to the mixture and allowed to stir under constant heating (55 °C) for 30 minutes, followed by the addition of 5 mL of 0.6 M ascorbic acid aqueous solution as reducing agent. The synthesis mixture was allowed to stir for 5 hours. The resulting nanoparticles were separated by washing them in DI water and ethanol three times each to remove all residue from the synthesis mixture. The washed and clean large Cu₂O spherical nanoparticles were then used in the photocatalytic experiments.

The synthesized Cu₂O spherical and cubical particles were characterized using UV-Vis-near IR extinction spectroscopy, X-ray diffraction (XRD) analysis, transmission electron microscopy (TEM), and scanning electron microscopy (SEM). All UV-Vis-near IR extinction spectra were taken using an Agilent Cary 60 Spectrophotometer. XRD patterns were acquired using a Philips X-Ray diffractometer (Phillips PW 3710 MPD, PW2233/20 X-Ray tube, Copper tube detector – wavelength - 1.5418 Angstroms), operating at 45 KW, 40 mA. The TEM images were taken using JEOL JEM-2100 TEM and Thermo Fisher Scientific Titan Themis 200 G2 aberration-corrected TEM. The JEOL JEM-2100 system is equipped with a LaB₆ gun and an accelerating voltage of

200 kV. The Titan Themis 200 system is equipped with a Schottky field-emission electron gun and operated at 200 kV.

II. Experimental procedure for performing photocatalytic experiments

Photocatalytic dye degradation reaction conditions: A 6 mL quartz tube and the Luzchem Exposure Panels provided with LED lamps (Figure S1f in SI) were used as a reaction chamber and the visible-light source, respectively. To measure the photocatalytic activity of small Cu₂O spheres and large Cu₂O cubes, the reaction mixture containing 1 mM concentration of MB and 5.8 mg of Cu₂O photocatalyst in 4 ml of solvent (dimethylformamide or ethanol) was first allowed to equilibrate at room temperature (~20 °C) for 3 hours in the dark. The reaction mixture was then sparged with air for 30 minutes to keep the soluble oxygen (O₂) content in the solvent same for all experiments. The equilibrated mixture under the stirring conditions at room temperature was then exposed to the visible light (i.e., blue and green LEDs). The intensity of this light source, when measured at the surface of the photoreactor, was 88,680 mW/m². To measure the extent of photodegradation of MB by small Cu₂O spheres and large Cu₂O cubes, the MB concentration (C) in the reaction mixture was quantified as a function of reaction time. The MB absorption value at its peak absorption wavelength (i.e., 665 nm) was used to quantify the MB concentration in the reaction mixture. More specific details are also provided below.

5.8 mg of Cu₂O nanocatalyst (spheres or cubes) is uniformly dispersed (sonicated for 2 minutes) in 4 mL of reaction solvent (dimethylformamide, DMF, or ethanol, EtOH). The mixture is added to a 6 mL quartz test tube (i.e., photoreactor). For experiments with benzoquinone, 43.2 mg (100 mM) of benzoquinone is added to the reaction mixture. 10 mM methylene blue (MB) solution is made in the same reaction solvent (DMF or EtOH) used for photocatalytic reaction. 150 μ L of 10 mM MB solution is added to the reaction mixture in the quartz test tube and allowed to stir at 1150 rpm and equilibrate at room temperature for three hours in the dark environment. The reactor is transferred to the Luzchem LED Panels (arranged with 4 Luzchem Exposure panels), where LED lamps can be attached as shown in Figure S1f. Sampling was done as a function of reaction time by taking 100 μ L of the reaction mixture and diluted in 4 mL dilution solvent (DMF or EtOH). Care was taken to make sure the reaction solvent and diluent are the same. These samples were characterized by UV-Vis to obtain absorption of methylene blue and corresponding C/C₀ values as a function of time were obtained. Incident light intensities were measured using Intell Pro Instruments Pro, Smart Sensor purchased from Luzchem Research Inc. The detector is placed exactly where the reactor is placed inside the Luzchem reactor (arranged with 4 Luzchem Exposure panels). Using the Smart sensor and AR823 Digital Lux meter (i.e., purchased from Luzchem Research Inc), the corresponding settings based on the wavelength range of the LED light intensity are measured in Lux. The values are converted to Light intensity in mW/m² by multiplying measured lux with the calibration factors.

III. Transient absorption measurements

Transient absorption measurements: Optical pump-probe experiments were performed using ~100 fs pulses from a 1-kHz laser amplifier, with a pump center wavelength of 400 nm and a probe center wavelength of 800 nm. Photoexcitation by the pump pulse is above the Cu₂O bandgap and created photoexcited charge carriers. The probe pulse determines the subsequent photocarrier

dynamics predominantly through free-carrier absorption. All samples are mixed with a ~1% concentration by mass into a KBr matrix and compressed into a semitransparent disc and measured at room temperature. More specific details are also provided below.

Transient absorption measurements were performed using ~100-fs pulses from a laser amplifier with a 1-kHz repetition rate. The amplifier emits pulses with a center wavelength of 800 nm, which are separated into two replica pulses, time-delayed with a mechanical translation stage with a total relative delay time of ~2 ns. The pump pulses are frequency-doubled in a β -barium borate crystal to 400-nm, so they have photon energy well above the bandgap of Cu₂O. The probe pulse remains at 800 nm, close to the band edge of the samples. The probe light transmits (and scatters) through the sample. Each transmission sample is a compressed disk, consisting of approximately 1% of the powdered sample in a KBr matrix, produced in a light vacuum for samples with lower scattering. At the samples, the pump beam has a $1/e^2$ diameter of ~0.35 mm and an average beam power of 1.12 mW, whereas the probe beam has a $1/e^2$ diameter of ~0.1 mm and an average beam power of 0.5 mW. Differential transmission data is recorded in a silicon photodetector, feeding a lock-in-amplifier that is referenced to a mechanical chopper placed in the pump beam and synchronized to a sub-harmonic of the laser amplifier.

IV. Details of finite-difference time-domain (FDTD) simulations

To implement FDTD simulations, we employed the Lumerical FDTD package.¹ The real (n) and imaginary (k) parts of the refractive indexes used in the simulations for Cu₂O, CeO₂, α -Fe₂O₃, and TiO₂ are shown in Table S1-S4, respectively. The perfectly matched layer (PML) boundary conditions were used for the simulations in all x, y, and z directions. The simulations were performed in a surrounding medium with a refractive index of 1. For the simulations of extinction, scattering, and absorption spectra, the respective cross sections as a function of wavelengths were calculated using the total-field/scattered-field (TFSF) formalism. The incident light source used for these simulations was the Gaussian source in the simulated wavelength region. On implementing the simulations of the magnetic and electric field distributions, a plane wave was used as electromagnetic field incidence with propagation in the x-axis direction, and polarization along the y-axis and the z-axis for the electric field and the magnetic field, respectively.

For the calculation of the normalized absorption cross section, we propose here a simple approximation to relate the photocatalytic rates to the optical and geometrical properties of metal oxide particles. This approximation is similar to the approximation proposed by Ingram et al². for understanding plasmonic resonance-enhanced photocatalysis. In our proposed approximation, the photocatalytic rate (r) at given incident light wavelength is proportional to the incident light intensity (I₀), the ratio of absorption cross section (σ_{acs}) to geometric cross section (G) of the particle, and surface to volume (S/V) ratio of the particle as shown in the equation below.

$$r \propto I_0 \times \sigma_{acs}/G \times S/V \quad (1)$$

When a constant incident light intensity is used as in our case of photocatalytic experiments with large Cu₂O cubes and small Cu₂O spheres, the above approximation can be written as: $r \propto \sigma_{acs}/G \times S/V$. Therefore, we define the normalized absorption cross section as normalized $\sigma_{acs} = \sigma_{acs}/G \times S/V$.

Supplementary Information Figures

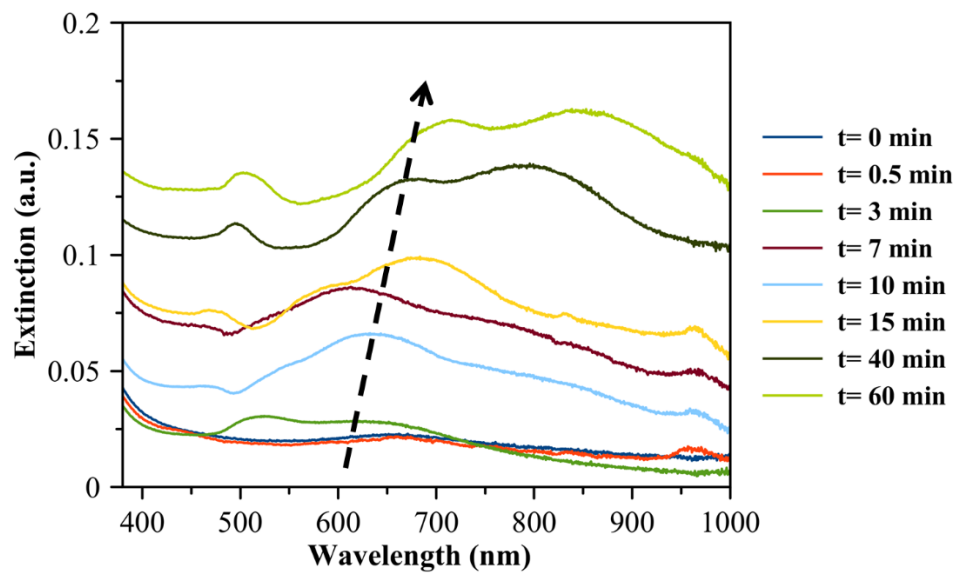


Figure S1a. Time-evolution of extinction spectra of Cu_2O cubes synthesized using chemical reduction method. The arrow shows the direction of synthesis time. The legends show the synthesis time.

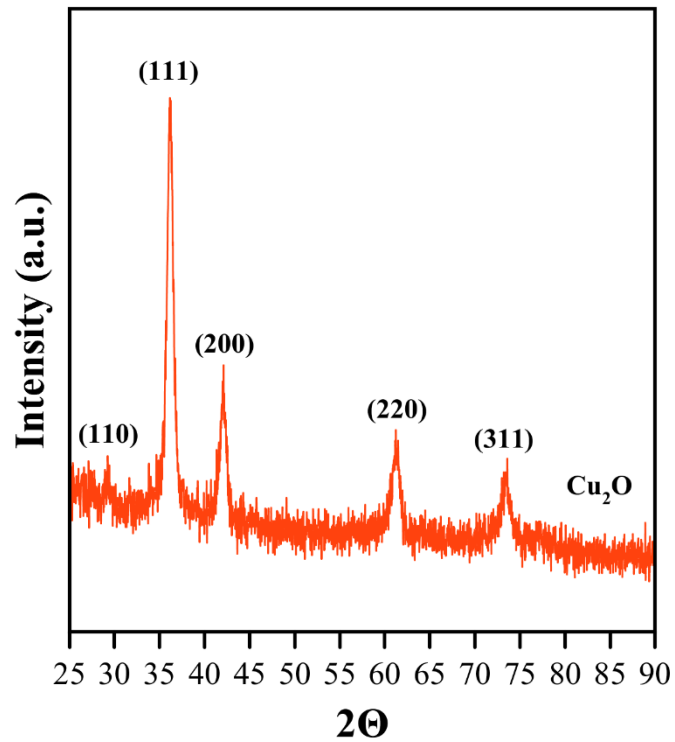


Figure S1b. Representative X-ray diffraction pattern of large Cu₂O cubes of 297 ± 38 nm edge length synthesized using chemical reduction method.

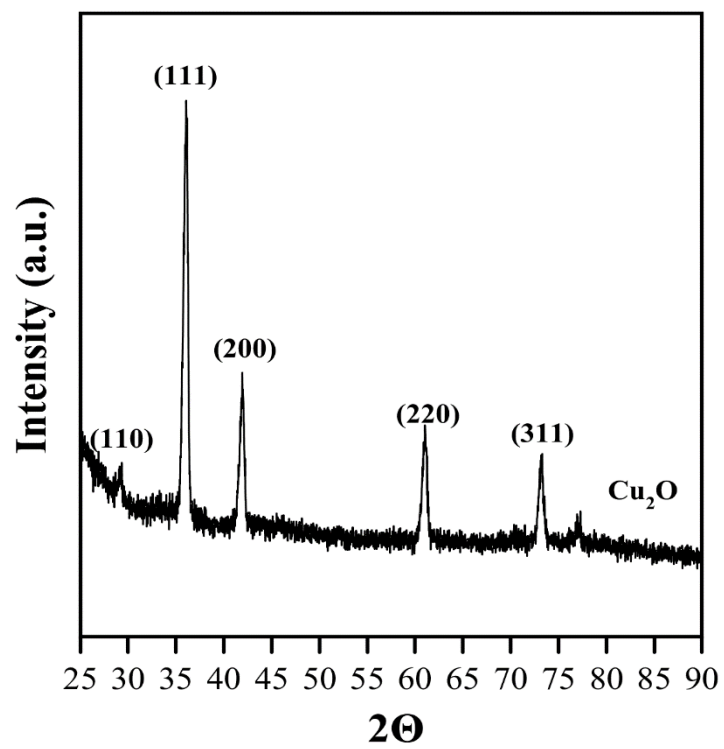


Figure S1c. Representative X-ray diffraction pattern of small Cu₂O spheres of 37 ± 6 nm diameter synthesized using microemulsion method.

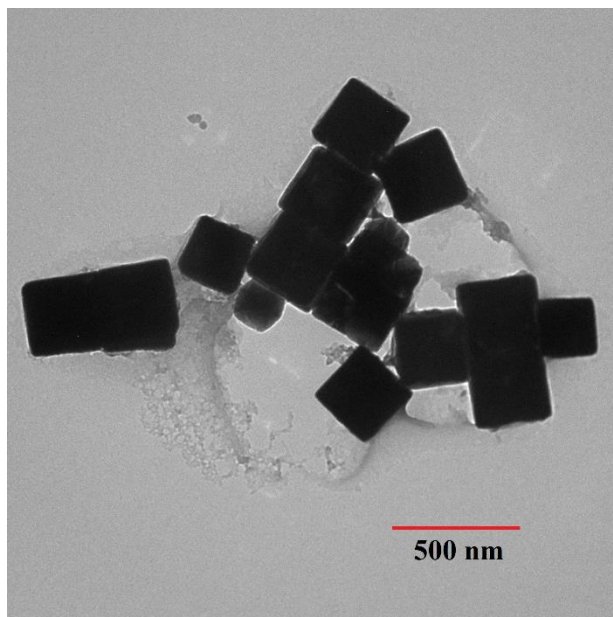


Figure S1d. Representative transmission electron microcopy image of large Cu₂O cubes of 297 ± 38 nm edge length synthesized using chemical reduction method.

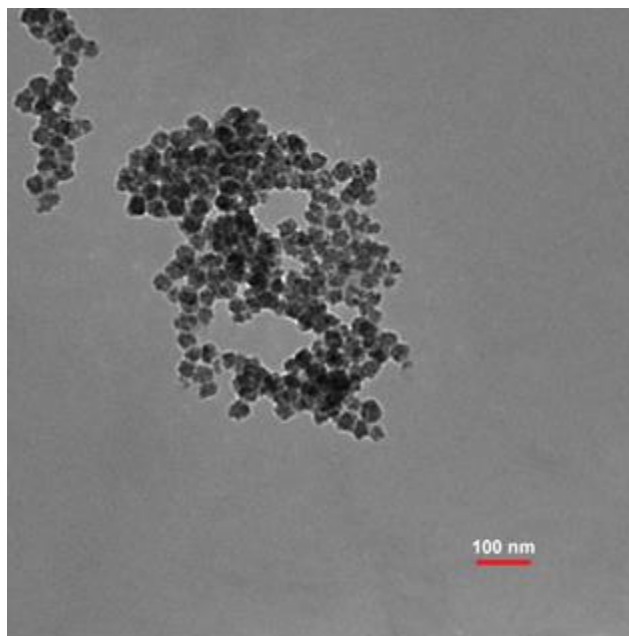


Figure S1e. Representative transmission electron microscopy image of small Cu_2O quasi-spherical particles of 37 ± 6 nm diameter synthesized using microemulsion method.

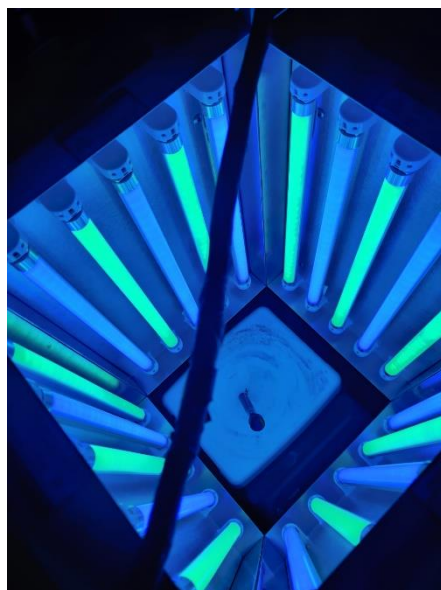


Figure S1f. Photoreactor reactor set up of Luzchem Exposure Panels connected with 10 blue and 10 green LED lamps.

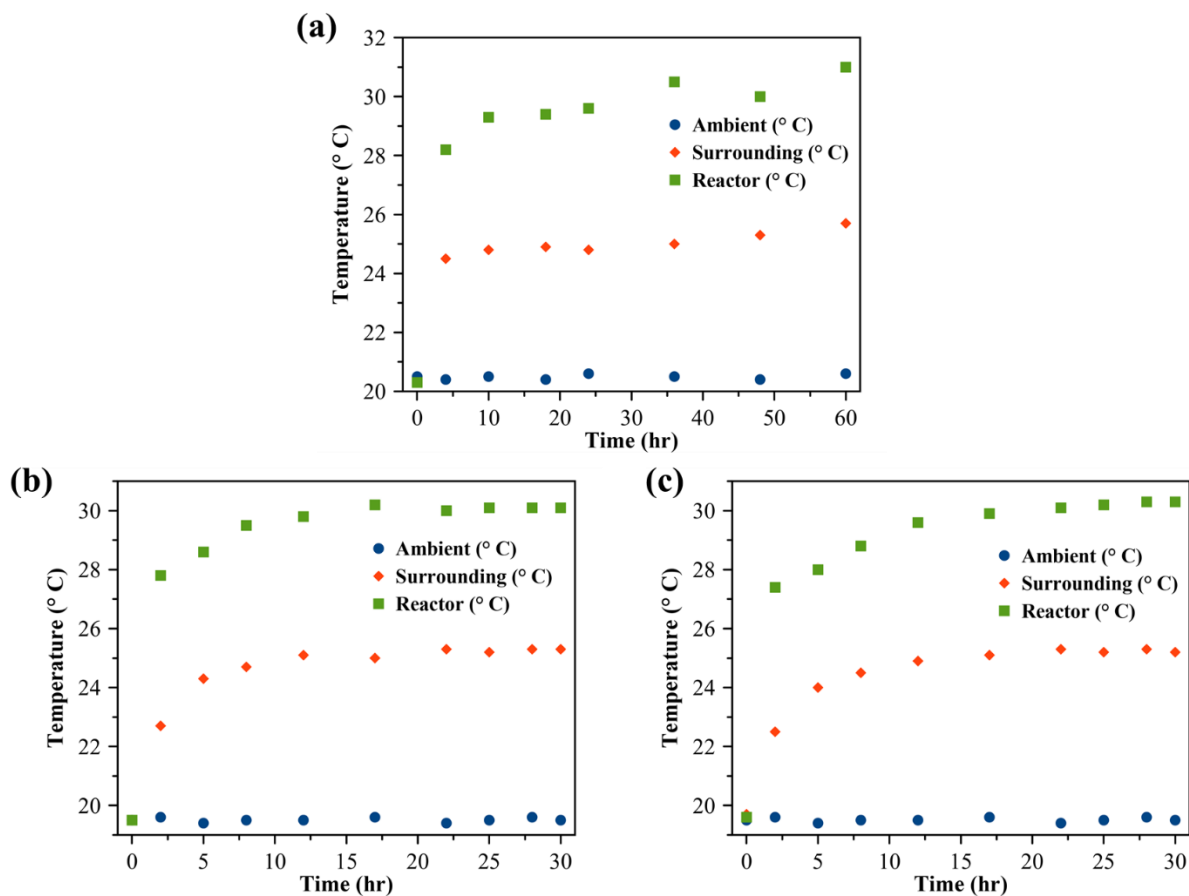


Figure S2a-c. Temperature profile measured as a function of irradiation time during photocatalytic degradation of MB in ethanol for different conditions: **(a)** blank conditions in the absence of photocatalyst, **(b)** using small Cu₂O nanospheres of 37 ± 6 nm diameter, **(c)** using large Cu₂O nanocubes of 297 ± 38 nm edge length. The data represented by green squares, red diamonds, and blue circles show the temperature of the sample in the photoreactor, temperature of the reactor surrounding, and ambient room temperature of the laboratory, respectively.

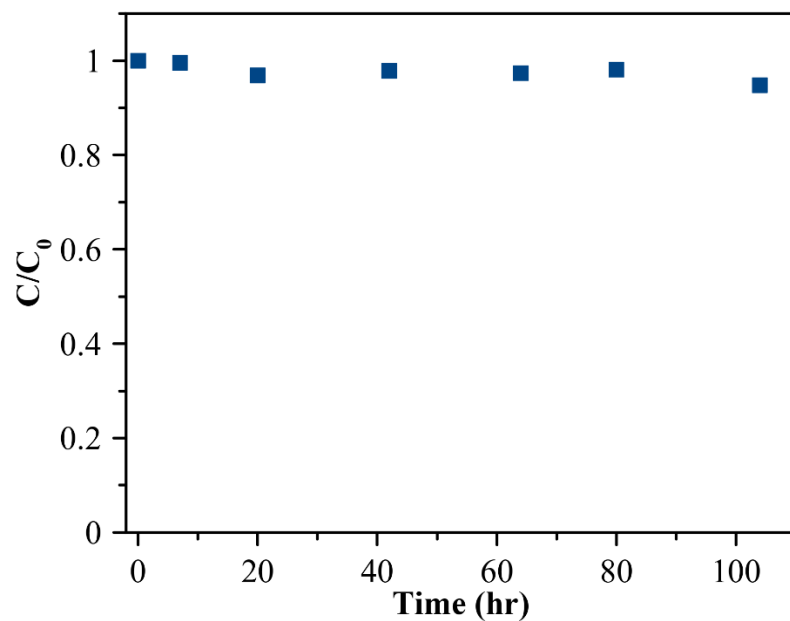


Figure S2d. Plot of C/C_0 of methylene blue versus reaction time measured during heating experiments at 60 °C in the presence of large Cu_2O cubes in ethanol under dark conditions (i.e., in the absence of LED light exposure).

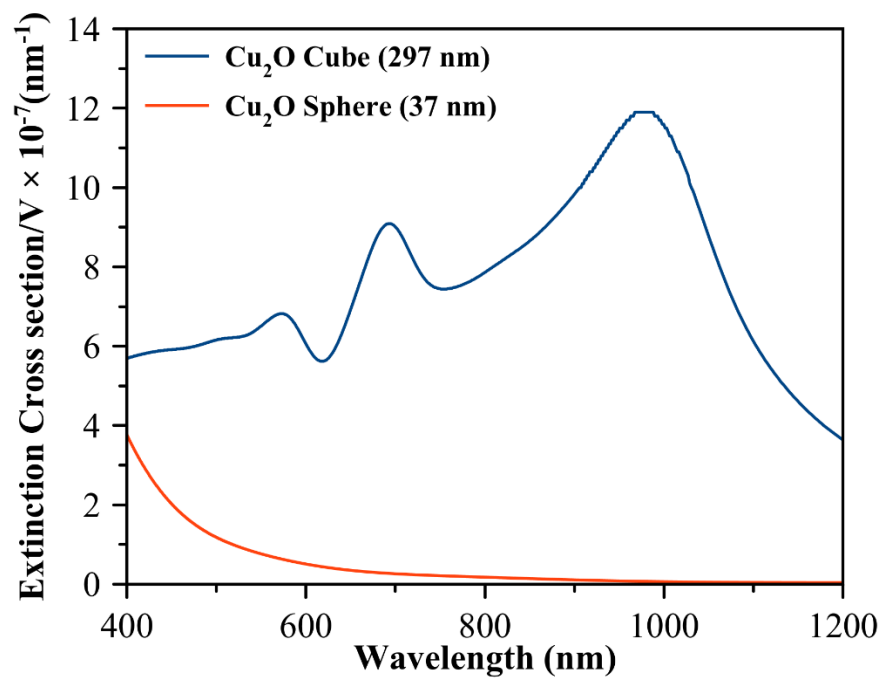


Figure S3a. FDTD-simulated volume-normalized extinction cross section of large Cu_2O nanocube of 297 nm edge length and small Cu_2O nanospheres of 37 nm diameter.

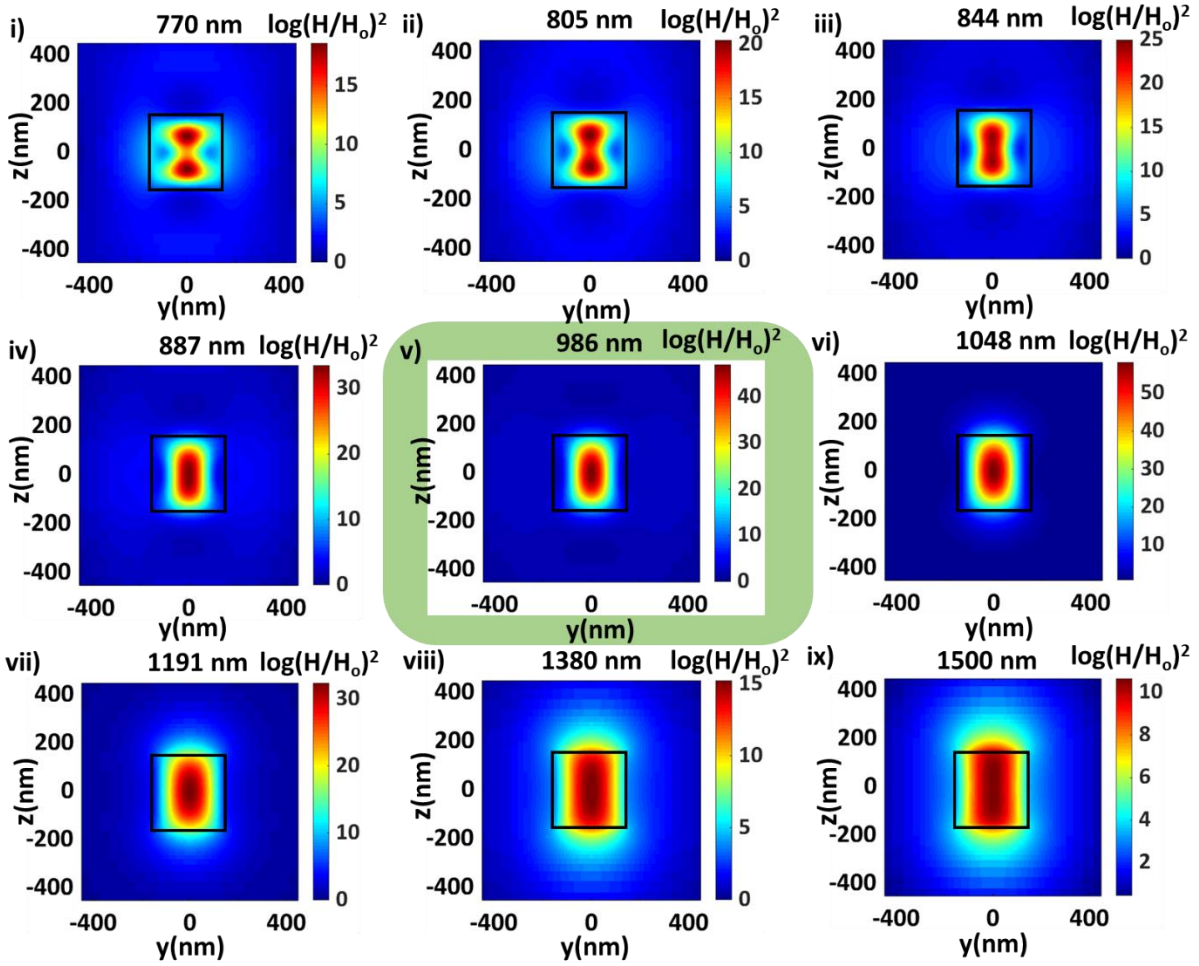


Figure S3b (I). FDTD-simulated spatial distribution of enhancement in magnetic field intensity $[H^2/H_0^2]$ in YZ plane at different wavelengths across the lowest energy Mie resonance peak wavelength (i.e., 986 nm) for Cu_2O cube of 297 nm edge length.

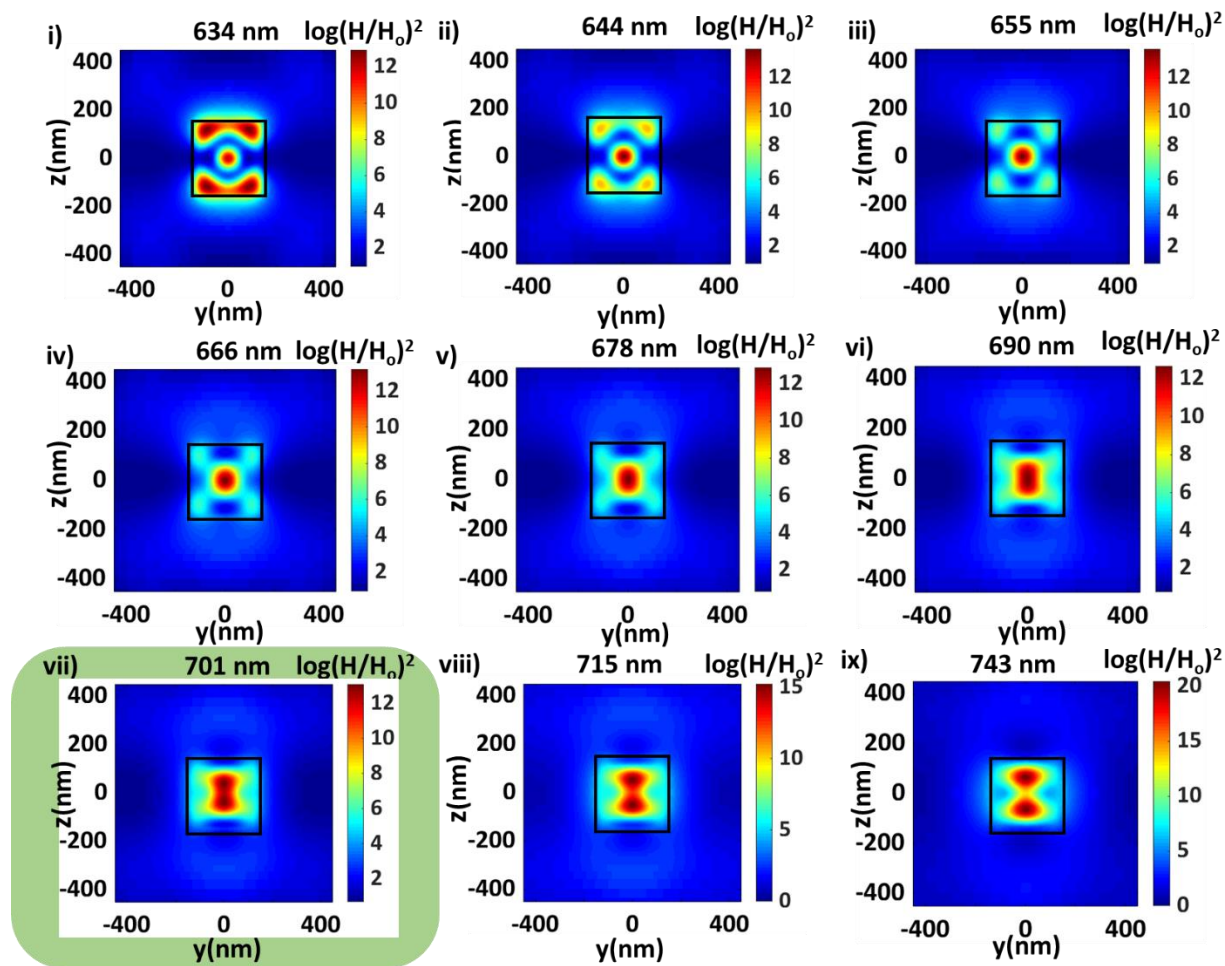


Figure S3b (II). FDTD-simulated spatial distribution of enhancement in magnetic field intensity $[H^2/H_0^2]$ in YZ plane at different wavelengths across the second lowest energy Mie resonance peak wavelength (i.e., 701 nm) for Cu_2O cube of 297 nm edge length.

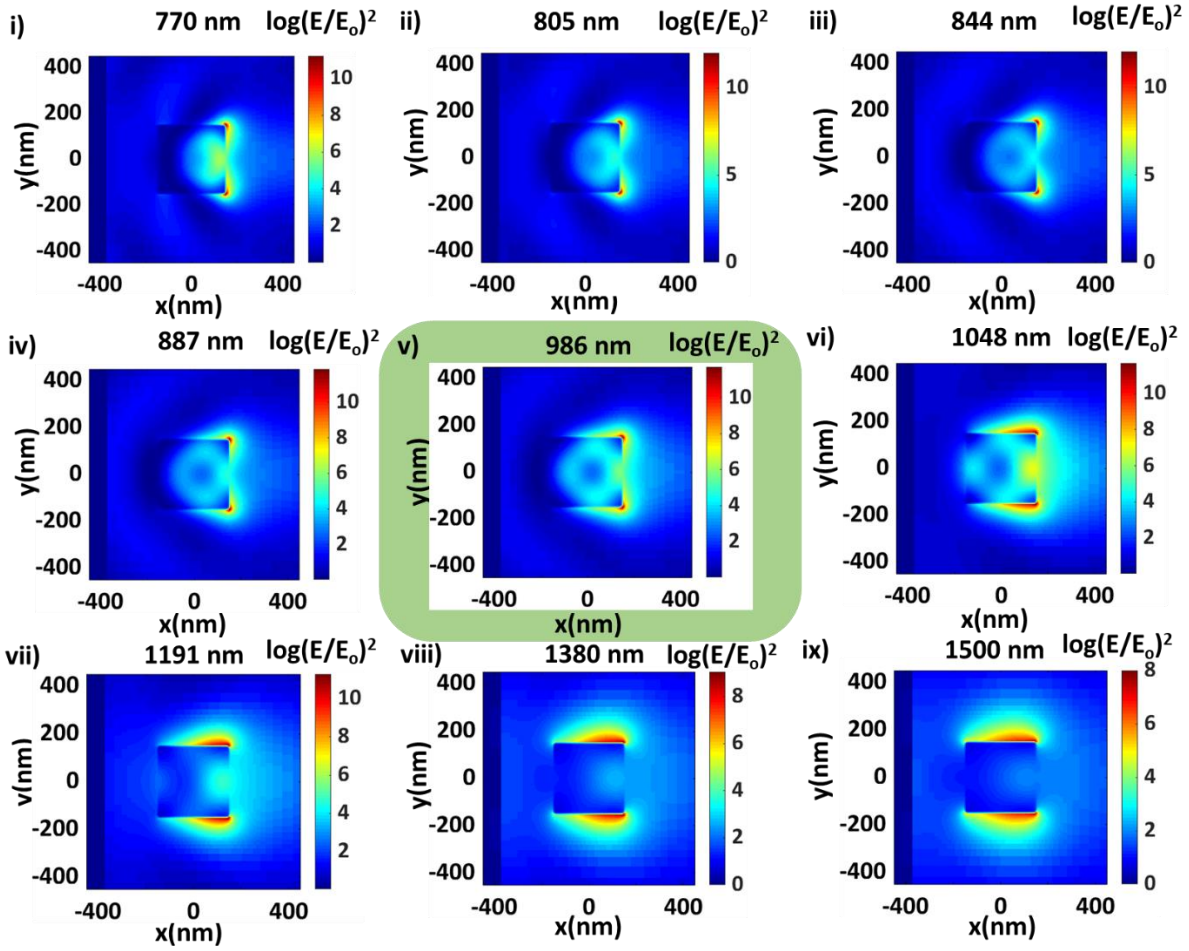


Figure S3c (I). FDTD-simulated spatial distribution of enhancement in electric field intensity $[E^2/E_0^2]$ in XY plane at different wavelengths across the lowest energy Mie resonance peak wavelength (i.e., 986 nm) for Cu_2O cube of 297 nm edge length.

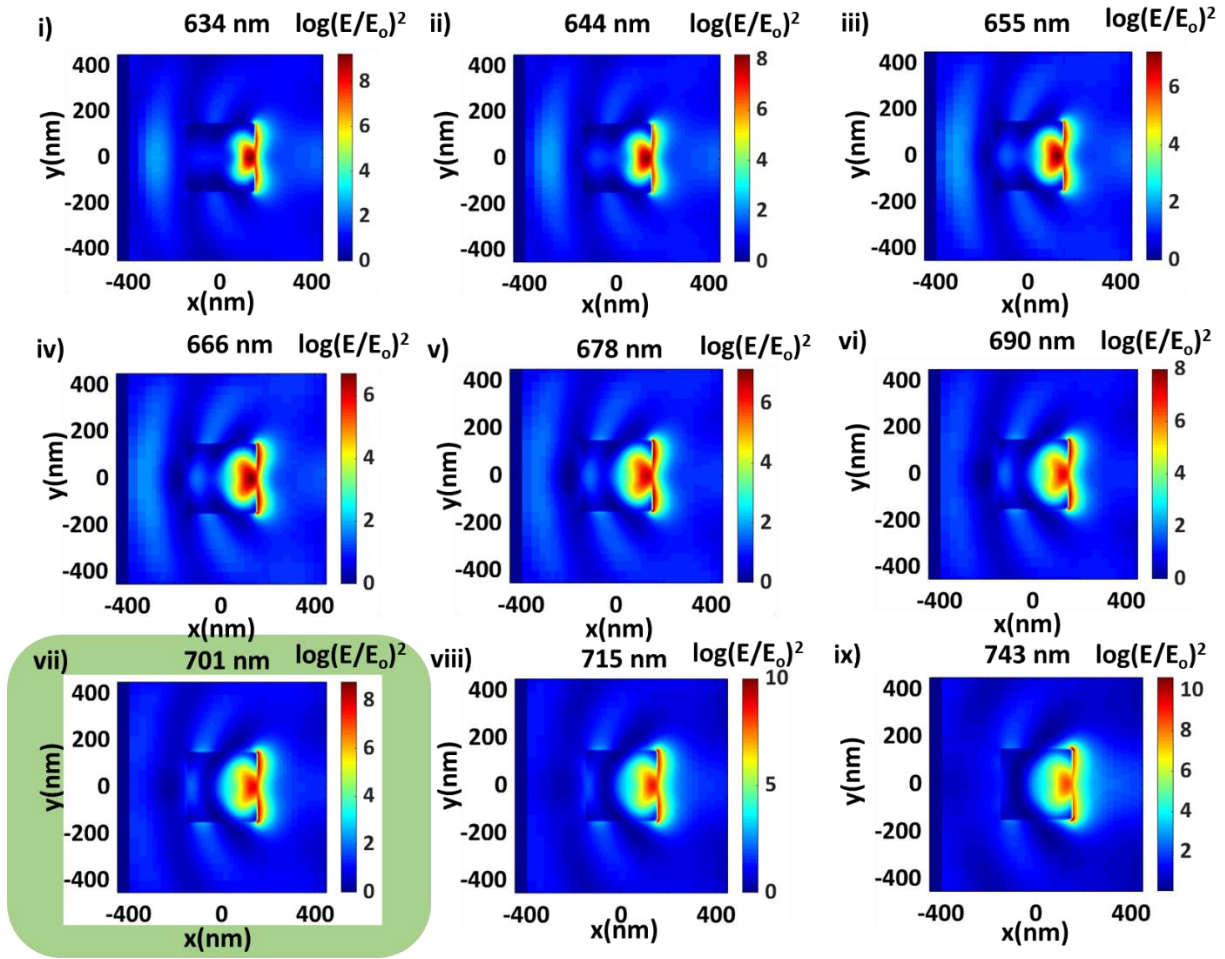


Figure S3c (II). FDTD-simulated spatial distribution of enhancement in electric field intensity $[E^2/E_0^2]$ in XY plane at different wavelengths across the second lowest energy Mie resonance peak wavelength (i.e., 701 nm) for Cu_2O cube of 297 nm edge length.

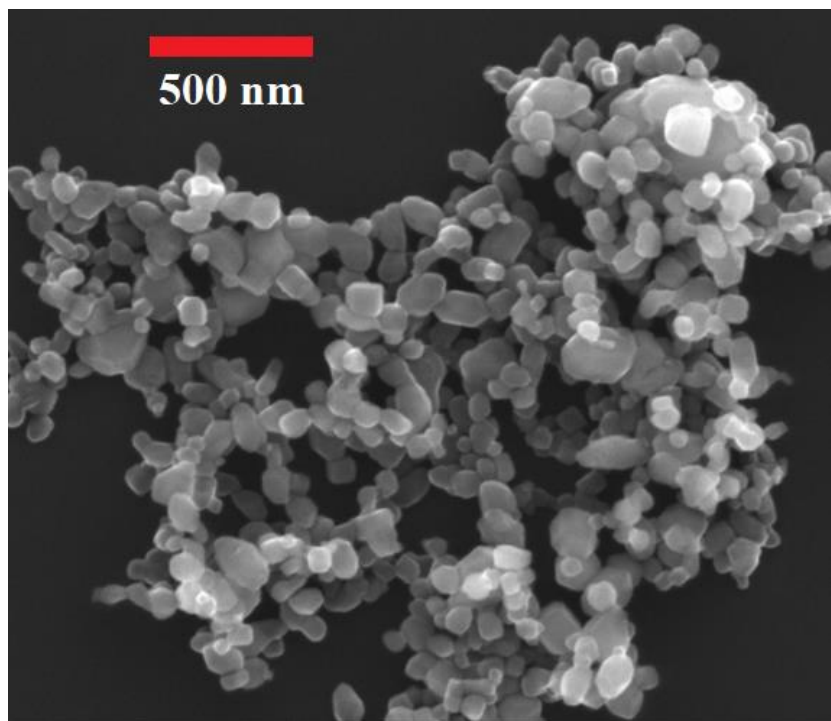


Figure S3d. Representative scanning electron microscopy image of large Cu₂O quasi-spherical particles of 115 ± 25 nm diameter synthesized using chemical reduction method.

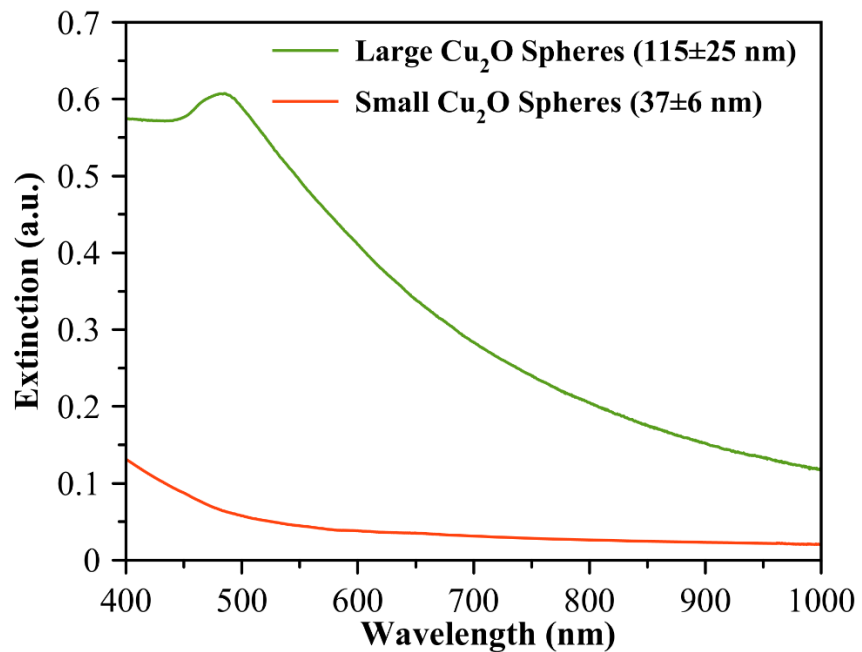


Figure S3e. Experimentally measured UV-Vis-near IR extinction spectra of large Cu₂O nanospheres of 115 ± 25 nm diameter and small Cu₂O nanospheres of 37 ± 6 nm diameter.

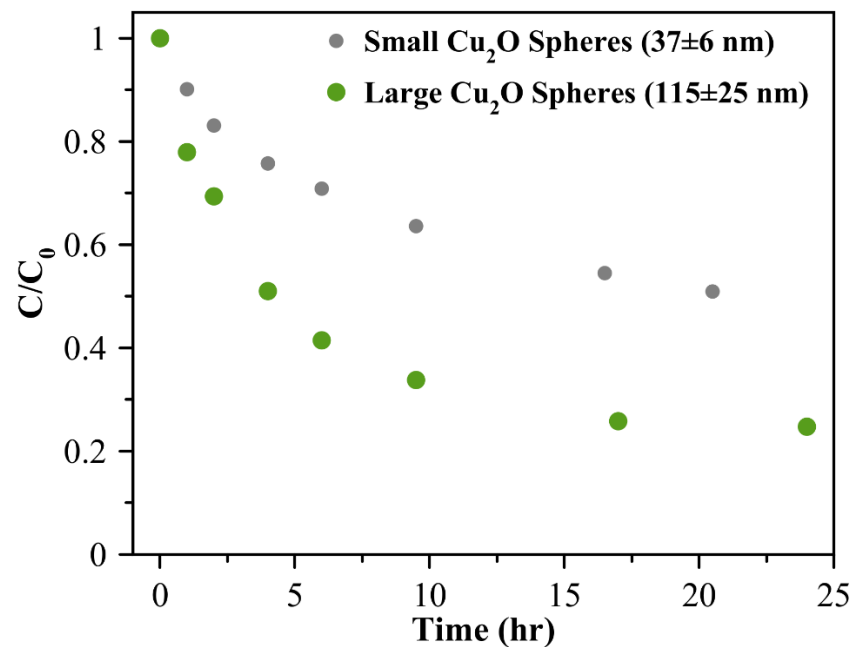


Figure S3f. Plot of C/C_0 versus irradiation time for photocatalytic degradation of MB in DMF using small Cu₂O nanospheres of 37 ± 6 nm diameter (grey circles) and large Cu₂O nanospheres of 115 ± 25 nm diameter (green circles) under green and blue LED illumination.

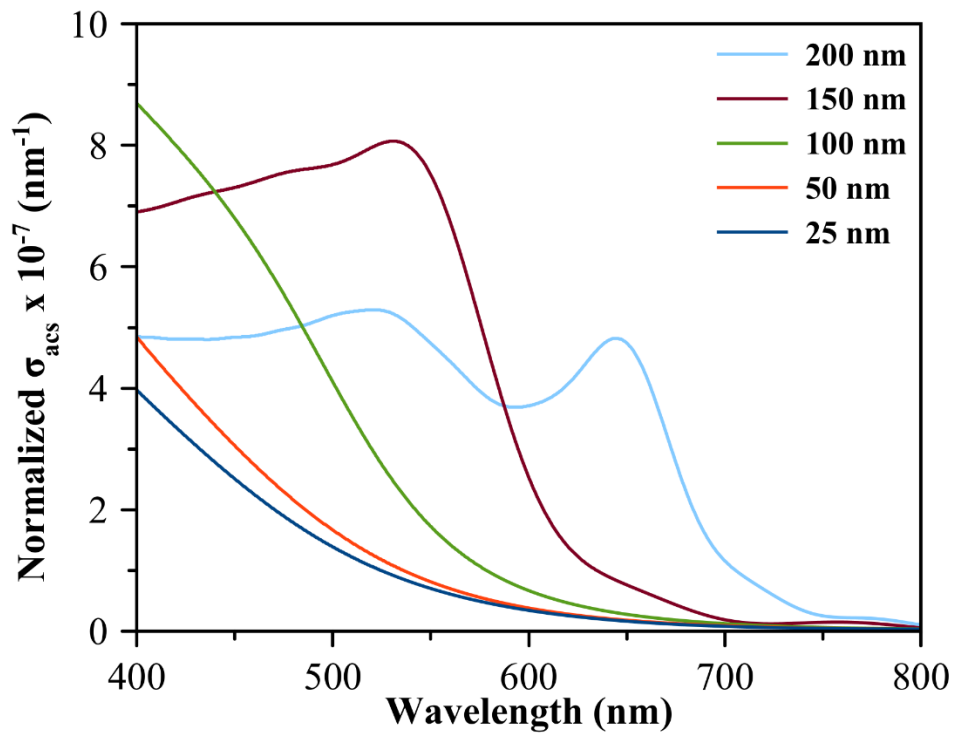


Figure S4a. FDTD-simulated normalized absorption cross section (normalized σ_{acs}) as a function of incident light wavelength for α -Fe₂O₃ spherical particles of different sizes. Normalized $\sigma_{acs} = \sigma_{acs}/G \times S/V$; where σ_{acs} , G, S, and V are absorption cross section, geometric cross section, surface area, and volume of the particle.

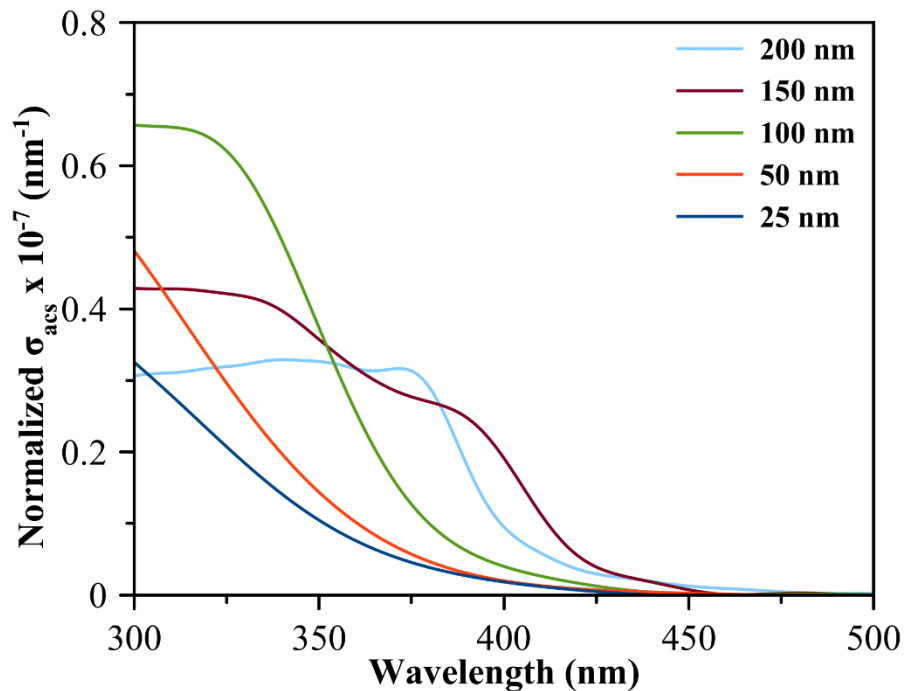


Figure S4b. FDTD-simulated normalized absorption cross section (normalized σ_{acs}) as a function of incident light wavelength for CeO_2 spherical particles of different sizes. Normalized $\sigma_{acs} = \sigma_{acs}/G \times S/V$; where σ_{acs} , G , S , and V are absorption cross section, geometric cross section, surface area, and volume of the particle.

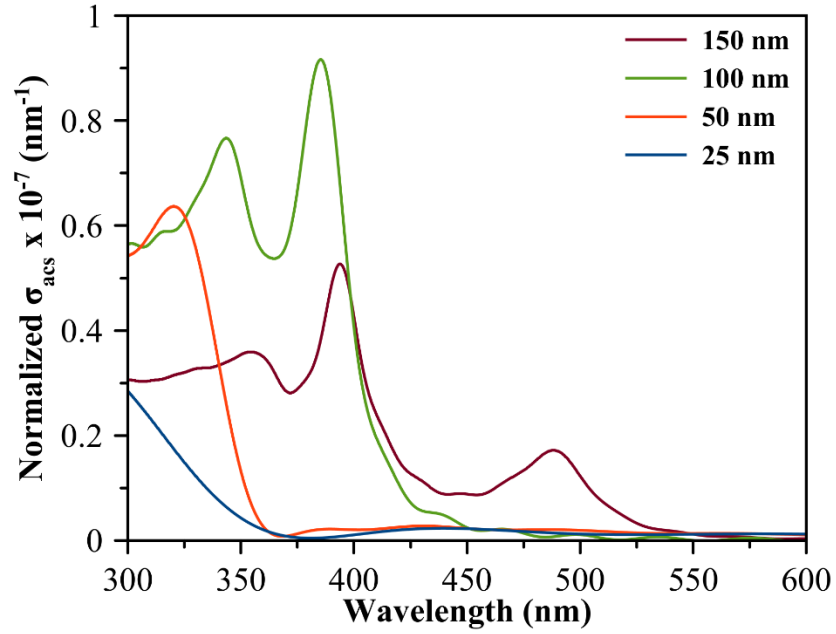


Figure S4c. FDTD-simulated normalized absorption cross section (normalized σ_{acs}) as a function of incident light wavelength for TiO₂ spherical particles of different sizes. Normalized $\sigma_{acs} = \sigma_{acs}/G \times S/V$; where σ_{acs} , G, S, and V are absorption cross section, geometric cross section, surface area, and volume of the particle.

Table S1. The real (n) and imaginary (k) parts of refractive index values of Cu₂O used in the simulations.³

	Cu₂O	
λ (nm)	n	k
300	2	1.85
350	2.4	1.44
400	2.8	0.99
450	3.06	0.6
500	3.12	0.35
550	3.1	0.19
600	3.02	0.13
650	2.9	0.1
700	2.83	0.083
750	2.77	0.07
800	2.7	0.06
850	2.66	0.053
900	2.63	0.048
950	2.61	0.043
1000	2.6	0.04
1100	2.59	0.033
1200	2.58	0.027
1300	2.57	0.021
1400	2.57	0.017
1500	2.57	0.013
2000	2.56	0.002

Table S2. The real (n) and imaginary (k) parts of refractive index values of CeO₂ used in the simulations.⁴

CeO₂											
λ (nm)	n	k	λ (nm)	n	k	λ (nm)	n	k	λ (nm)	n	k
401	2.47	0.11	624	2.16	0.00	854	2.13	0.00	929	2.12	0.00
410	2.41	0.08	635	2.15	0.00	864	2.13	0.00	940	2.12	0.00
421	2.38	0.03	646	2.15	0.00	876	2.13	0.00	951	2.12	0.00
429	2.36	0.02	657	2.15	0.00	886	2.13	0.00	962	2.11	0.00
439	2.31	0.01	668	2.15	0.00	897	2.12	0.00	973	2.11	0.00
450	2.29	0.01	679	2.15	0.00	908	2.12	0.00	984	2.11	0.00
461	2.28	0.00	690	2.15	0.00	919	2.12	0.00	996	2.11	0.00
471	2.25	0.00	701	2.15	0.00	929	2.12	0.00	929	2.12	0.00
483	2.24	0.00	712	2.14	0.00	940	2.12	0.00	940	2.12	0.00
494	2.22	0.00	722	2.15	0.00	951	2.12	0.00	951	2.12	0.00
504	2.21	0.00	733	2.15	0.00	962	2.11	0.00	962	2.11	0.00
516	2.20	0.00	744	2.14	0.00	973	2.11	0.00	973	2.11	0.00
526	2.19	0.00	755	2.14	0.00	984	2.11	0.00	984	2.11	0.00
537	2.18	0.00	766	2.14	0.00	996	2.11	0.00	996	2.11	0.00
548	2.18	0.00	777	2.14	0.00	854	2.13	0.00	929	2.12	0.00
559	2.18	0.00	788	2.14	0.00	864	2.13	0.00	940	2.12	0.00
570	2.18	0.00	799	2.13	0.00	876	2.13	0.00	951	2.12	0.00
581	2.17	0.00	810	2.14	0.00	886	2.13	0.00	962	2.11	0.00
592	2.16	0.00	821	2.13	0.00	897	2.12	0.00	973	2.11	0.00
602	2.16	0.00	831	2.13	0.00	908	2.12	0.00	984	2.11	0.00
613	2.16	0.00	842	2.13	0.00	919	2.12	0.00	996	2.11	0.00

Table S3. The real (n) and imaginary (k) parts of refractive index values of α -Fe₂O₃ used in the simulations.⁵

λ (nm)	α -Fe ₂ O ₃	
	n	k
400	2.756	1.294
450	3.181	1.02
500	3.282	0.675
550	3.318	0.498
600	3.265	0.149
650	3.074	0.057
700	2.972	0.031
750	2.903	0.021
800	2.853	0.02
850	2.824	0.027
900	2.805	0.024
950	2.789	0.022
1000	2.775	0.015
1050	2.759	0.011
1100	2.745	0.011
1150	2.734	0.01
1200	2.723	0.011

Table S4. The real (n) and imaginary (k) parts of refractive index values of TiO₂ used in the simulations.^{6,7}

TiO₂								
λ (nm)	n	k	λ (nm)	n	k	λ (nm)	n	k
180	1.37	1.998	330	5.291	1.5698	480	3.08	0.0001
190	1.535	1.831	340	4.969	1.0926	490	3.054	0.0001
200	1.536	1.696	350	4.477	0.6508	500	3.03	0.0001
210	1.46	1.65	360	3.87	0.251	510	3.014	0.0001
220	1.433	1.806	370	3.661	0.033	520	3	0.0001
230	1.443	2.084	380	3.498	0.0001	530	2.985	0.0001
240	1.363	2.454	390	3.375	0.0001	540	2.97	0.0001
250	1.365	2.847	400	3.286	0.0001	550	2.954	0.0001
260	1.627	3.197	410	3.225	0.0001	560	2.94	0.0001
270	1.952	3.432	420	3.186	0.0001	570	2.929	0.0001
280	3.355	3.561	430	3.162	0.0001	580	2.92	0.0001
290	3.835	3.535	440	3.149	0.0001	590	2.91	0.0001
300	4.732	3.28	450	3.141	0.0001	600	2.9	0.0001
310	5.235	2.734	460	3.13	0.0001	610	2.889	0.0001
320	5.391	2.076	470	3.104	0.0001	620	2.88	0.0001

TiO₂								
λ (nm)	n	k	λ (nm)	n	k	λ (nm)	n	k
630	2.875	0.0001	780	2.8	0.0001	930	2.759	0.0001
640	2.87	0.0001	790	2.794	0.0001	940	2.76	0.0001
650	2.86	0.0001	800	2.79	0.0001	950	2.761	0.0001
660	2.85	0.0001	810	2.79	0.0001	960	2.76	0.0001
670	2.844	0.0001	820	2.79	0.0001	970	2.755	0.0001
680	2.84	0.0001	830	2.785	0.0001	980	2.75	0.0001
690	2.835	0.0001	840	2.78	0.0001	990	2.749	0.0001
700	2.83	0.0001	850	2.78	0.0001	1000	2.75	0.0001
710	2.825	0.0001	860	2.78	0.0001	1010	2.75	0.0001
720	2.82	0.0001	870	2.775	0.0001	1020	2.749	0.0001
730	2.814	0.0001	880	2.77	0.0001	1030	2.749	0.0001
740	2.81	0.0001	890	2.77	0.0001	1040	2.748	0.0001
750	2.81	0.0001	900	2.77	0.0001	1050	2.747	0.0001
760	2.81	0.0001	910	2.765	0.0001	1060	2.747	0.0001
770	2.806	0.0001	920	2.76	0.0001	1070	2.746	0.0001

TiO ₂								
λ (nm)	n	k	λ (nm)	n	k	λ (nm)	n	k
1080	2.745	0.0001	1230	2.729	0.0001	1380	2.721	0.0001
1090	2.744	0.0001	1240	2.729	0.0001	1390	2.721	0.0001
1100	2.742	0.0001	1250	2.728	0.0001	1400	2.72	0.0001
1110	2.741	0.0001	1260	2.728	0.0001	1410	2.719	0.0001
1120	2.74	0.0001	1270	2.727	0.0001	1420	2.719	0.0001
1130	2.739	0.0001	1280	2.727	0.0001	1430	2.718	0.0001
1140	2.738	0.0001	1290	2.726	0.0001	1440	2.717	0.0001
1150	2.737	0.0001	1300	2.726	0.0001	1450	2.716	0.0001
1160	2.736	0.0001	1310	2.725	0.0001	1460	2.715	0.0001
1170	2.735	0.0001	1320	2.725	0.0001	1470	2.714	0.0001
1180	2.734	0.0001	1330	2.724	0.0001	1480	2.713	0.0001
1190	2.733	0.0001	1340	2.724	0.0001	1490	2.711	0.0001
1200	2.732	0.0001	1350	2.723	0.0001	1500	2.71	0
1210	2.731	0.0001	1360	2.723	0.0001			
1220	2.73	0.0001	1370	2.722	0.0001			

References Cited in Supporting Information

- (1) Lumerical Inc. <http://www.lumerical.com/tcad-products/fdtd/> (accessed 2016 -09 -28).
- (2) Ingram, D. B.; Christopher, P.; Bauer, J. L.; Linic, S. Predictive Model for the Design of Plasmonic Metal/Semiconductor Composite Photocatalysts. *ACS Catal.* **2011**, *1* (10), 1441–1447. <https://doi.org/10.1021/cs200320h>.
- (3) Palik, E. D. *Handbook of Optical Constants of Solids*; Academic Press, 1998.
- (4) Hass, G.; Ramsey, J. B.; Thun, R. Optical Properties and Structure of Cerium Dioxide Films. *J. Opt. Soc. Am.* **1958**, *48* (5), 324. <https://doi.org/10.1364/JOSA.48.000324>.
- (5) Ordal, M. A.; Bell, R. J.; Alexander, R. W.; Long, L. L.; Querry, M. R. Optical Properties of Fourteen Metals in the Infrared and Far Infrared: Al, Co, Cu, Au, Fe, Pb, Mo, Ni, Pd, Pt, Ag, Ti, V, and W. *Appl. Opt.* **1985**, *24* (24), 4493. <https://doi.org/10.1364/AO.24.004493>.
- (6) Siefke, T.; Kroker, S.; Pfeiffer, K.; Puffky, O.; Dietrich, K.; Franta, D.; Ohlídal, I.; Szeghalmi, A.; Kley, E.; Tünnermann, A. Materials Pushing the Application Limits of Wire Grid Polarizers Further into the Deep Ultraviolet Spectral Range. *Adv. Opt. Mater.* **2016**, *4* (11), 1780–1786. <https://doi.org/10.1002/adom.201600250>.
- (7) Sarkar, S.; Gupta, V.; Kumar, M.; Schubert, J.; Probst, P. T.; Joseph, J.; König, T. A. F. Hybridized Guided-Mode Resonances via Colloidal Plasmonic Self-Assembled Grating. *ACS Appl. Mater. Interfaces* **2019**, *11* (14), 13752–13760. <https://doi.org/10.1021/acsami.8b20535>.